

**MODELING, SIMULATION, AND CONTROL OF TETHERED SPACE
DEBRIS**

by

Liam Field

August 31, 2022

A thesis submitted to the
Faculty of the Graduate School of
the University at Buffalo, State University of New York
in partial fulfilment of the requirements for the
degree of

Master of Science

Department of Mechanical and Aerospace Engineering

Copyright by

Liam Field

2022

All Rights Reserved

Dedication

To grandma.

Acknowledgments

I would like to thank my research advisor Dr. Botta for her patience and indelible feedback. I'm grateful for her guidance, without which this effort surely would have been impossible. My thanks also go out to my family for their perpetual support in all ways.

Abstract

Space debris poses a considerable risk to the continued safety of the near Earth orbital environment. To mitigate the growth in debris population, removal of large debris objects such as inactive satellites has been proposed. A promising removal method involves a flexible tethered-net, which provides a physical connection between an active craft and debris. This strong dynamic coupling and high flexibility presents unique dynamics and safety concerns for the removal mission. The intention of this work is to provide a basis for the analysis of the attitude motion of debris under the influence of the tether. Two models are described for simulation of the post-capture tethered removal scenario. The first model consists of a point mass chaser, a rigid debris, and a tether discretized using lumped parameters. This model is used to investigate the effects a lumped parameter tether model has on the chaser-target relative and debris attitude motions compared to a massless tether. The lumped parameter model is shown to display negligible effects on the target attitude motion while the chaser is thrusting. The system behavior after the thrust is shut off indicates that lumped parameters should be used if there is possible winding or end body collision. After this, a relative distance PID controller was designed to mitigate the negative effects a constant thrust had on the system motion. It is shown to successfully maintain a relative distance while failing to moderate the debris

attitude motion. The final part of this work involves validation of orbital mechanics in a commercial simulation engine. The results proved to be accurate, permitting the future development of a post-capture tethered-net simulator.

Table of Contents

Acknowledgments	iv
Abstract	v
List of Tables	ix
List of Figures	x
Chapter 1	
Introduction	1
Chapter 2	
System Modeling	7
2.1 Introduction	7
2.2 Point Mass Chaser and Rigid Target	7
2.2.1 Body Kinematics and Dynamics	8
2.2.2 Tether Model	9
2.2.3 Validation	11
2.3 Rigid Chaser and Target	15

2.3.1 Validation	17
Chapter 3	
Impact of Tether Discretization on Target Attitude Motion	21
3.1 Introduction	21
3.2 Simulations	21
Chapter 4	
Chaser Controls	28
4.1 Introduction	28
4.2 Chaser Attitude Control	28
4.3 Relative Distance PID Control	31
4.3.1 Tuning of PID Gains	33
4.3.2 Comparison of PID and Open Loop Performance	35
4.3.3 Saturation of Control Input	38
Chapter 5	
Vortex-Studio-Based Simulator Validation	45
5.1 Introduction	45
5.2 Vortex Studio Engine	46
5.3 Validation	47
Chapter 6	
Conclusion	50
Bibliography	53

List of Tables

2.1	System Parameters.	12
2.2	Initial conditions for the validation of the point chaser and rigid target model.	12
2.3	RMSE with respect to baseline simulation and simulation run times. . .	15
2.4	Initial conditions for the rigid chaser model validation (Section 2.3). . .	18
2.5	System Parameters for the rigid chaser model.	19
2.6	RMSE between chaser and target positions of Model 1 and Model 2 simulations.	20
5.1	RMSE with respect to baseline simulation.	49

List of Figures

2.1	Chaser, target, and tether models, ECI and body-fixed reference frames.	8
2.2	Validation results with <i>ode15s</i> and relative tolerance 10^{-5} for the initial conditions and system parameters of Hovell and Ulrich.	13
2.3	Elongations for the <i>ode45</i> and <i>ode15s</i> solvers with relative tolerance 10^{-9} for the initial conditions and system parameters of Hovell and Ulrich.	15
2.4	Chaser, target, and tether models, with relevant frames.	16
2.5	Simulation results with <i>ode45</i> and relative tolerance 10^{-9} . Model 1 and Model 2 are those described in Sections 2.2 and 2.3, respectively.	19
3.1	Results for case 1: tether slightly tensioned initially.	23
3.2	Results for case 2: tether -1 m slack initially	25
3.3	Image of system at $t = 50$ s in the chaser LVLH frame. The target is green, the chaser black, and the nodes blue. The lines connecting these are the tether segments, shown in two colors: red for tensioned and black for slack.	26
4.1	Sliding mode control results.	31

4.2	Negative initial elongation with varying gains.	34
4.3	Results comparison of PID and open loop for 1 m initial slack.	36
4.4	Results comparison of PID and open loop for 0.01 m initial slack.	39
4.5	Results for different saturation levels.	40
4.6	Target applied moment and angular acceleration for different saturation levels.	44
5.1	System in Vortex with chaser on the left, target on the right, and distance joint connecting them. The axes at either end of the joint are its attachment point axes.	48
5.2	Vortex and MATLAB simulation results of the model in Section 2.3.	49

Chapter 1

Introduction

Modern communications and research relies heavily on the operational safety of the near Earth space. With an estimated more than 36,000 debris objects larger than 10 cm and many tens of thousands of smaller objects in low earth orbit¹, the orbital environment is increasingly threatened by debris [1]. Beyond their own immediate danger to active satellites and future launches, collisions between debris objects pose a major threat. A cascade event in which the frequency of debris collisions, and the subsequent increase in the number of debris objects, supersedes the rate by which debris leaves orbit through the atmosphere was predicted by Kessler and Cour-Palais [2]. The exponential growth rate of these collisions makes it imperative to limit their occurrences.

The debris risk from new and future satellites can be mitigated by post mission disposal techniques, while old, inactive bodies (satellites and expended rockets) pose a considerable risk should a collision occur [3]. An example of such a collision occurred between the Iridium 33 and Cosmos 2251 satellites, which produced a large debris cloud [4]. Therefore, removal of large debris should be a priority for mitigation. Active debris removal (ADR) is the catch-

¹Estimates courtesy of ESA: www.esa.int/Space_Safety/Space_Debris/Space_debris_by_the_numbers

all term for methods, processes, and technologies whose mission is to remove debris through active interference with the debris objects. ADR missions involve an active craft which can interact with the debris. There are two key approaches when using an active craft: contactless and contact interaction. In contactless methods, no physical connection exists between the active craft and debris. Proposed methods utilize lasers [5] or ion beams [6] produced from ion engines to change the debris velocity and ultimately cause atmospheric reentry. In contrast, contact methods involve a physical interaction between active craft and debris. The vast majority utilize a robotic effector [7, 8] or flexible tether [9, 10, 11, 12, 13] as the primary linkage and momentum transmission connection. Compared to contactless methods, contact methods provide a shorter mission timescale, which is pivotal to mitigating debris increases [14]. In particular, tether-based methods provide a greater degree of safety and economy compared to other contact removal methods [15].

For tether-based removal methods, the ADR mission can be broken down into four broad phases: (1) rendezvous, (2) capture, (3) detumbling, and (4) removal. The rendezvous phase involves the launch and approach of the active craft (chaser) to the debris (target), such that it can carry out its means of interaction. The capture phase involves the successful linking of chaser and target through the tether. The actual means of capture is via a net [11, 16, 17], harpoon [9, 18, 19, 20], or robotic gripper [21, 22]. Tethered-nets are launched at the target, opening such that the target can be contained within the net's internal volume. Harpoons, on the other hand, are launched directly at the target to penetrate and embed in its surface. Capture with a robotic gripper is different, as it must carefully grip the target to prevent unwanted collisions. In the third phase, which occurs immediately after capture, the residual angular momen-

tum of the target must be dissipated [22, 23, 24, 25]. The target may be tumbling before the capture, and the capture itself might induce angular motion of the target [26]. Finally, the removal phase of the mission involves the deorbiting of the target, either by placement in a graveyard orbit (from GEO) or atmospheric reentry of the chaser-target stack (from LEO). For the capture phase, tethered-nets provide some distinct advantages over other contact-based methods. They require lower precision compared to harpoons or grippers, which require precise maneuvers to effectively attach to the target [27]. Tethered-nets are also applicable to a variety of target geometries [28]. Net capture has also been performed in an on-orbit demonstration mission as part of ESA's RemoveDEBRIS experiment, albeit in the absence of a tether, indicating promise for debris capture missions [29].

The tethered-net removal system, while providing benefits in the capture phase, poses its own unique challenges for phases 3 and 4 due to the highly flexible nature of the system. The primary means of force transmittance, the tether, can only sustain tension, complicating control of the system. Particularly, collision of the chaser and target must be avoided. Aslanov showed that attitude motion of the target is particularly important, as it can result in unwanted behavior such as winding [30] or chaos in the tether libration angle [31]. As such, the focus of this research is in the post-capture phases of the mission, where the complex tethered dynamics are emergent. In particular, there is a focus on the debris angular motion subject to the chaser-tether motion.

In order to get an understanding of the effectiveness of the tethered-net removal system, numerical simulations must be performed. In the post-capture phases, the net is often unmodeled due to its low inertia properties and computational complexity [23, 32], which can become prohibitive for the long du-

ration of detumbling and deorbiting. Usually, the tether-net is replaced by a single tether, rigidly pinned to the surface of the debris [23, 32, 33, 34, 35, 36, 37]. While the collision of the net and subsequent impulse on the debris is lost, this modeling strategy permits preliminary assessments of the impacts of the tether parameters and the design of controllers for the system. As the central component of the system, the tether model must be accurate. Given that the tether is a flexible body, the most accurate solutions for its spatial behavior would be derived from partial differential equations. However, a Kelvin-Voigt spring-damper model for the tether has been used extensively in the post-capture scenario due to its simple implementation [32, 33, 36, 37]. Modeling the tether as a massless spring-damper necessarily results in the loss of fidelity of its transverse motion. A remedy for this is discretizing the tether with lumped masses. The lumped mass model was investigated in [38], where it was found that modeling increasing numbers of lumped masses in the tether increases the amplitude of transverse oscillations during a burn maneuver. Sabatini et al. showed that discretization allows tension to propagate along the tether, as would occur in the real physical tether [39]. As the attitude motion of debris can affect the system dynamics, it is important to understand the effects discretization can have on debris attitude motion.

Maintaining a relative distance between the chaser and target is critically important for the success of the mission. Aslanov and Yudintsev showed that slackness of the tether is a major contributor for tether winding about the target [30], which can result in mission failure. To counter the possibility of tether winding, Meng et al. developed an impedance-based tension controller by regulating the natural length of the tether via a reel mechanism, effectively controlling the relative distance [40]. Benvenuto et al. showed that a burn maneu-

ver can cause a possible collision of the chaser and target, as left uncontrolled they approach closely [41]. Jasper and Schaub utilized open loop input shaping of the chaser thrust to reduce the risk of a collision after a Δv maneuver [42]. Jaworski et al. developed a PID control which was able to maintain a relative distance in the tether as well as stabilize the target attitude motion [35, 43]. Wave-based control of the chaser to track a reference velocity for deorbiting was implemented by Cleary and O'Connor [34]. They showed that the controller was successful in keeping the tether tensioned, with the system stabilizing at the tether natural length after the maneuver.

This work intends to further illuminate the modeling and simulation of the post-capture dynamics of a tether-based active debris removal system. Using lumped parameters in the tether can model its transverse behavior; however, it is also necessary to understand the dynamics impacts of modeling with a varying number of lumped parameters. A model of the ADR scenario with a discretized tether, subject to a constant thrust, will be simulated to see how much the system dynamics change by varying the number of lumped masses. This will be directly compared to a massless tether, to confirm that this baseline modeling of the tether captures the overall system behavior, with a particular focus on the target attitude motion and target-chaser relative motion. A relative distance PID controller will be introduced to maintain a tension in the tether, as this results in a more controllable target. The effects on the system dynamics of this controller will be compared to using a constant thrust. Further development of tethered-based simulators – including the net – for the post-capture phases of the mission is necessary to advance work in estimation, control, and post-capture dynamics analysis. A simulator that was previously built for net-based capture by Botta et al. [16], will be expanded for use in the post-capture phase.

The remainder of this thesis is organized as follows. Chapter 2 introduces the models of the chaser-tether-target system which will be used for generating results. Chapter 3 presents an analysis of the effects of tether discretization on the system dynamics, and in particular its impact on the debris attitude. In Chapter 4, a relative distance PID controller is introduced and its performance is compared to an open-loop controller. Chapter 5 presents the validation of a chaser-tether-target simulator for the post-capture phase under orbital mechanics in Vortex Studio, which is a stepping stone for future research. Finally, Chapter 6 concludes the work with a discussion of the contributions and future directions of this research.

Chapter **2**

System Modeling

2.1 Introduction

In this chapter, two models representing the post-capture scenario are described. Validation of the models is discussed here as well.

2.2 Point Mass Chaser and Rigid Target

The first model analyzed consists of a point mass chaser satellite, a rigid target satellite, and a tether discretized using N lumped masses, such that the number of tether segments is $N + 1$ (see Fig. 2.1). The chaser is modeled as a point mass as it is assumed to have its own, perfect, attitude control. The target is modeled as a rectangular prism. In Fig. 2.1, the Earth-Centered Inertial reference frame is indicated by $\mathcal{O} = [\hat{\mathbf{I}}, \hat{\mathbf{J}}, \hat{\mathbf{K}}]$, while the body-fixed frame of the target is defined as $\mathcal{T} = [\hat{\mathbf{x}}, \hat{\mathbf{y}}, \hat{\mathbf{z}}]$. The vector ${}^T\mathbf{r}_{tp,T}$ is the tether attachment point on the target in frame \mathcal{T} .

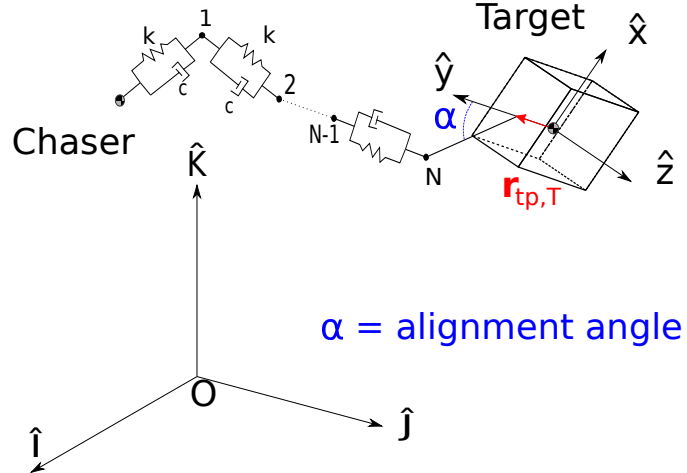


Figure 2.1: Chaser, target, and tether models, ECI and body-fixed reference frames.

2.2.1 Body Kinematics and Dynamics

The translational kinematics of the bodies are described by the position, \mathbf{R} , and the velocity, \mathbf{V} , of the given body's center of mass (c.o.m.) in the ECI frame. The rotational kinematics of the target are described by the quaternion, \mathbf{q} , and angular rate, $\boldsymbol{\omega}$. The attitude quaternion for the target body is expressed in the ECI frame as $\mathbf{q} = [q_0, q_1, q_2, q_3]^T$ where q_0 and $[q_1, q_2, q_3]^T$ are the scalar and vector components, respectively. The target angular velocity is expressed in \mathcal{T} as $\boldsymbol{\omega} = [\omega_x, \omega_y, \omega_z]^T$. The translational and rotational kinematic relationships are

$$\dot{\mathbf{R}} = \mathbf{V} \quad (2.1)$$

$$\dot{\mathbf{q}} = \frac{1}{2} \begin{bmatrix} -q_1 & -q_2 & -q_3 \\ q_0 & -q_3 & q_2 \\ q_3 & q_0 & -q_1 \\ -q_2 & q_1 & q_0 \end{bmatrix} \begin{bmatrix} \omega_x \\ \omega_y \\ \omega_z \end{bmatrix} = \frac{1}{2} Q(\mathbf{q}) \boldsymbol{\omega} \quad (2.2)$$

The matrix $Q(\mathbf{q})$ is composed of the target quaternion and is the same as the explicitly written quaternion kinematics matrix. The translational equations of motion for all bodies, including the tether lumped masses (referred to as nodes from here), are

$$m\ddot{\mathbf{R}} = -m\mu \frac{\mathbf{R}}{|\mathbf{R}|^3} + \sum \mathbf{T} + \mathbf{F} \quad (2.3)$$

where m is the mass of the body, μ is the standard gravitational parameter of Earth ($3.986 \cdot 10^5 \text{ km}^3/\text{s}^2$), $\sum \mathbf{T}$ is the sum of the tensions in the tethers connected to the body, and \mathbf{F} is the resultant of all other external forces on the body. As the only external forces modeled are gravity and the tether tension, \mathbf{F} is zero for all bodies other than the chaser when control forces are present. The angular equations of motion for the target are expressed in the target body frame as

$$\dot{\boldsymbol{\omega}} = J_T^{-1}({}^\mathcal{T}\mathbf{r}_{tp,T} \times {}^\mathcal{T}A^O \mathbf{T} - \boldsymbol{\omega} \times J_T \boldsymbol{\omega}) \quad (2.4)$$

where J_T is the inertia matrix for the target. The transformation matrix ${}^\mathcal{T}A^O$ is needed to transform tension forces from the ECI frame to the target body-fixed frame. As the tether is rigidly connected to the target, ${}^\mathcal{T}\mathbf{r}_{tp,T}$ is constant in the target body frame.

2.2.2 Tether Model

The tether is modeled as a series of spring-damper elements, discretized using N lumped masses. The tether mass is evenly distributed to the end bodies of each of the $N + 1$ tether segments (mass points, target and chaser). The segment mass is calculated from the tether's physical properties, where the seg-

ment mass m_s is found as

$$m_s = \rho A_t l_t (N + 1)^{-1} \quad (2.5)$$

The tether density, cross-sectional area, and natural length are ρ , A_t , and l_t , respectively. Twisting and bending of the tether are not modeled at this time. To incorporate the tether's inability to support compression, the tension in a segment of the tether is calculated by

$$\mathbf{T}_i = \begin{cases} T_i \hat{\mathbf{e}}_i & \text{if}(l_i > l_0) \wedge (T_i > 0), \\ 0 & \text{if}(l_i \leq l_0) \vee (T_i \leq 0). \end{cases} \quad (2.6)$$

with $T_i = k_s(l_i - l_0) + c_s \dot{l}_i$ where k_s and c_s are the stiffness and damping constants of a segment, l_0 is the segment natural length, and l_i and \dot{l}_i are the i -th tether segment's instantaneous length and length rate. The segment heading vector $\hat{\mathbf{e}}_i$ is given by

$$\hat{\mathbf{e}}_i = \frac{\mathbf{R}_{i+1} - \mathbf{R}_i}{\|\mathbf{R}_{i+1} - \mathbf{R}_i\|} \quad (2.7)$$

where \mathbf{R}_i and \mathbf{R}_{i+1} indicate the positions of tether nodes in the order indicated in Fig. 2.1, with $\mathbf{R}_i = \mathbf{R}_C$ for $i = 1$ and $\mathbf{R}_{i+1} = \mathbf{R}_T + {}^{\mathcal{O}}A^{\mathcal{T}\mathcal{T}}\mathbf{r}_{tp,T}$ for $i = N + 1$ (attachment point on the target), if \mathbf{R}_C and \mathbf{R}_T are the positions of the chaser and target's centers of mass. The tether segment lengths, l_i , are the denominators of e_i . The segment velocities \dot{l}_i are found by taking the relative velocity between the two end bodies of the segment, then projecting this onto e_i , giving the one dimensional tether rate of change:

$$\dot{l}_i = (\mathbf{V}_{i+1} - \mathbf{V}_i) \cdot \hat{\mathbf{e}}_i \quad (2.8)$$

For $i = N + 1$, $\mathbf{V}_{i+1} = \mathbf{V}_T +^{\mathcal{O}} \mathbf{A}^T \boldsymbol{\omega} \times^T \mathbf{r}_{tp,T}$. The stiffness and damping coefficients of the tether segments are defined based on the tether nodes N , the Young's Modulus of the tether material E , and the tether cross-sectional area as:

$$k_s = \frac{EA_t(N+1)}{l_t} \quad (2.9)$$

$$c_s = c(N+1) \quad (2.10)$$

where c is the tether damping coefficient for $N = 0$.

2.2.3 Validation

The model described in the previous section is validated by visual comparison to the results in Hovell and Ulrich [33]. In that work, a model consisting of a rigid target, a spring-damper tether, and point mass chaser is investigated. The comparison is performed against the results present in Section 5.A of that work, specifically the single tether configuration (i.e. the same model as described here with $N = 0$). There is also an open loop thrust applied to the chaser, \mathbf{F}_{OL} , with a magnitude of 20 N, F_{OL} , fired in the negative chaser velocity direction:

$$\mathbf{F}_{OL} = -F_{OL} \frac{\mathbf{V}_C}{\|\mathbf{V}_C\|} \quad (2.11)$$

Considering the model is easily formulated as ordinary differential equations, MATLAB's built-in solvers were chosen to validate the model. The results were almost exactly reproduced using the *ode15s* solver, with a relative tolerance of 10^{-5} . The initial conditions and system parameters for the simulation are given in Tables 2.1 and 2.2, respectively. With these initial conditions, the tether is slightly tensioned and the target has an in orbital plane angle of $\frac{\pi}{6}$

Table 2.1: System Parameters.

Parameter	Value
Target Inertia Matrix J_T (kg-m ²)	diag(15000, 3000, 15000)
Target Attachment Point ${}^T r_{tp,T}$ (m)	$[0, -0.875, 0]^T$
Chaser Mass m_C (kg)	500
Target Mass m_T (kg)	3000
Young's Modulus E (GPa)	60
Tether Area A (mm ²)	0.784
Tether Damping c (Ns/m)	16
Tether Natural Length l_t (m)	30
Number of nodes N	0

Table 2.2: Initial conditions for the validation of the point chaser and rigid target model.

Variable	Value
R_C (m)	$[-6176011.04, -42079.219, 2973766.46]^T$
R_T (m)	$[-6176020.96, -42080.997, 2973743.40]^T$
V_C (m/s)	$[-2457.79535, -4404.28547, -5712.40584]^T$
V_T (m/s)	$[-2457.76467, -4404.28338, -5712.420604]^T$
q_T (-)	$[-0.85286853, 0.15038373, -0.08682409, 0.49240388]^T$
ω_T (rad/s)	$[0, .05, 0]^T$

rad with respect to the tether. The chaser is placed behind the target in the orbit, in the direction opposite the system velocity. This is the correct orientation for towing the debris towards the atmosphere, as the chaser can reduce the system velocity. The total run time is 6000 s.

Figure 2.2a shows the tether elongation, which is presented to display the longitudinal behavior of the tether. The target angular rates and alignment angle are also presented in Figures 2.2c and 2.2b, respectively. They provide a measure of the tumbling motion of the target and therefore the safety of the removal process. The alignment angle (α in Figure 2.1) is the angle between the tether heading vector and the outward facing normal of the attachment face:

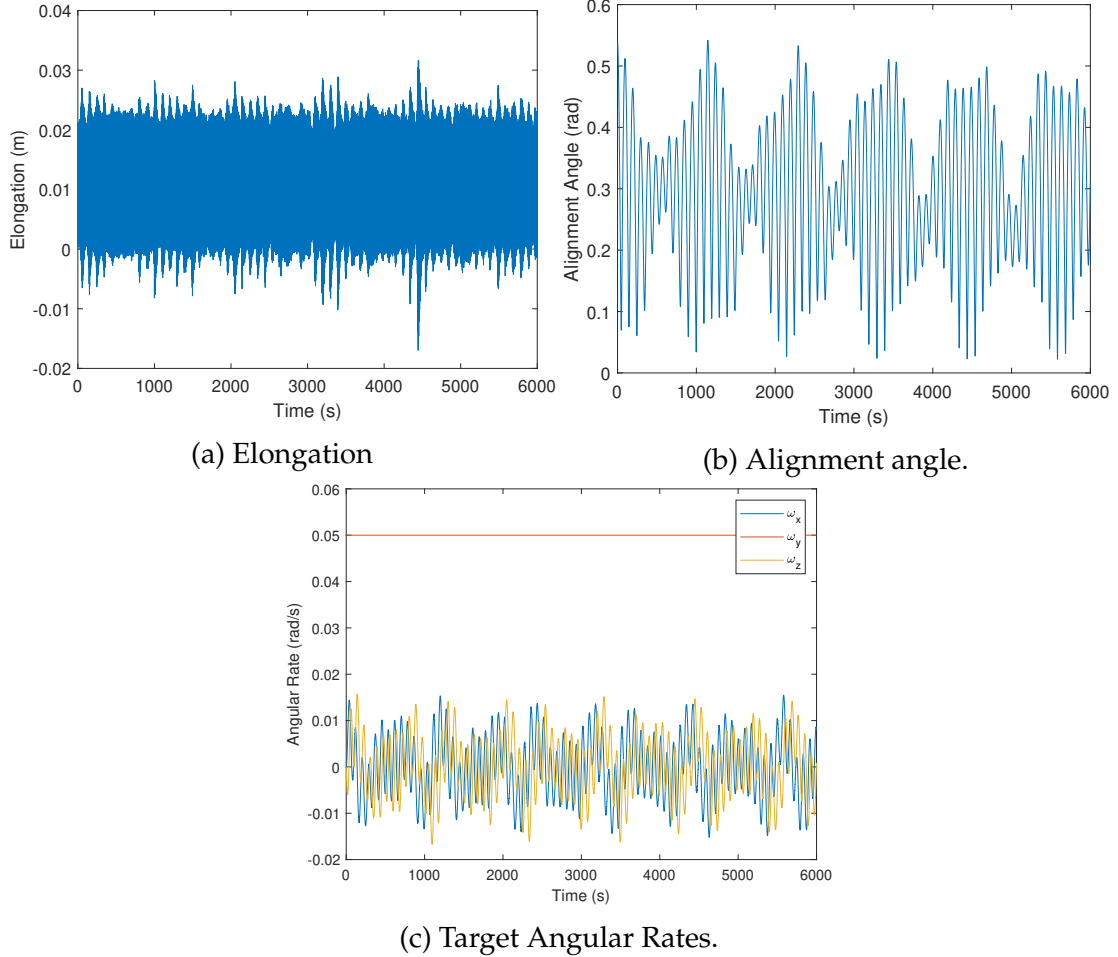


Figure 2.2: Validation results with *ode15s* and relative tolerance 10^{-5} for the initial conditions and system parameters of Hovell and Ulrich.

$$\alpha = \arccos \frac{-\hat{\mathbf{e}}_{N+1} \cdot \mathcal{O} \mathbf{r}_{tp,T}}{\| -\hat{\mathbf{e}}_{N+1} \| \cdot \| \mathcal{O} \mathbf{r}_{tp,T} \|} \quad (2.12)$$

An angle greater than $\frac{\pi}{2}$ rad indicates a collision between the target and tether, which can lead to winding of the tether about the target and possible mission failure. Some important behavior of the system should be noted before continuing. Firstly, ω_y is unchanging due to the choice of attachment point, and secondly, the tether alignment angle is slowly decreasing to an equilibrium point. While the chosen solver accurately reproduces the results, issues lay in the re-

sults themselves. The elongation shows no signs of reaching an equilibrium state, despite the not insignificant damping value. To resolve this, three further simulations with the same initial conditions and parameters were performed. The first simulation used *ode15s*, with a new relative tolerance of 10^{-9} . The two others were performed using *ode45* with tolerances of 10^{-5} and 10^{-9} . The performance measure between the simulations is the root mean square error (RMSE) in the target and chaser positions. The simulation data produced using *ode15s* with a tolerance of 10^{-5} was chosen as the baseline simulation, as it was validated by reproducing the results of Hovell and Ulrich. The RMSE is then found using the formula:

$$RMSE = \left(\frac{1}{n} \sum_{j=1}^n (x_j - x_{j,r})^2 + (y_j - y_{j,r})^2 + (z_j - z_{j,r})^2 \right)^{\frac{1}{2}} \quad (2.13)$$

where j denotes the timestep and n is the number of data points. The x , y and z terms are the components of the inertial position vector for either the chaser or target, such that $\mathbf{R} = [x, y, z]^T$. The subscript r denotes the baseline simulation values for the same inertial position. Table 2.3 contains the RMSE for the chaser and target positions, as well as the total run time of each simulation. The RMSE values, on the order of 10^1 m, indicate a significant deviation from the baseline simulation. In fact, the three additional simulations produce results much more similar to each other than to the baseline. Additionally, *ode45* proved to be much faster in completing the simulation. The issue of the tether elongation is resolved by the tolerance of 10^{-9} . This is depicted in Figure 2.3, where the tether elongation of both solvers with the lower tolerance are displayed. While the *ode15s* elongation oscillations do reduce in amplitude, there are still significant deviations throughout the simulation (e.g. at $t = 4340$ s). The *ode45* elongation

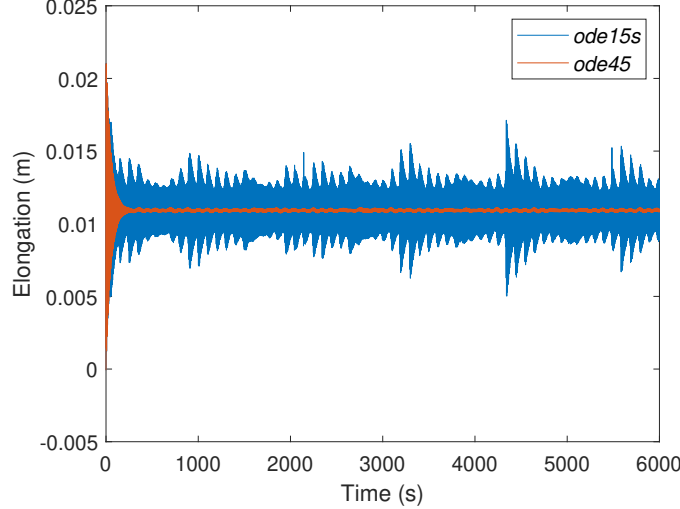


Figure 2.3: Elongations for the *ode45* and *ode15s* solvers with relative tolerance 10^{-9} for the initial conditions and system parameters of Hovell and Ulrich.

gation considerably reduces in amplitude, slightly oscillating at around 0.0109 m towards the end of the simulation. From this result and the reduction in run time, it's clear the *ode45* solver with a relative tolerance of 10^{-9} is favorable for simulation of this model.

Table 2.3: RMSE with respect to baseline simulation and simulation run times.

Solver	Tolerance	Chaser (m)	Target (m)	Run Time (s)
ode15s	10^{-5}	-	-	4.5805
	10^{-9}	29.7517	29.7529	3.6011
ode45	10^{-5}	29.8299	29.8310	0.8181
	10^{-9}	29.8299	29.8310	0.7434

2.3 Rigid Chaser and Target

The model described in this section consists of a chaser and target, both rigid bodies, and a flexible tether connection. The target and tether model - here without lumped masses- are the same as described in Section 2.2. By making

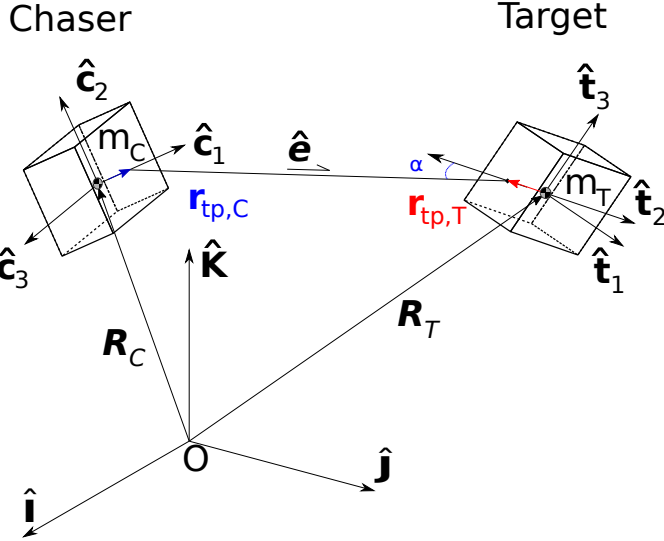


Figure 2.4: Chaser, target, and tether models, with relevant frames.

the chaser a rigid body, the model only slightly changes and allows for the introduction of chaser attitude control. The chaser has its own body frame, $\mathcal{C} = [\hat{c}_1, \hat{c}_2, \hat{c}_3]$, and the target body frame definition has been adjusted to $\mathcal{T} = [\hat{t}_1, \hat{t}_2, \hat{t}_3]$, both depicted in Figure 2.4. The inertial frame \mathcal{O} remains the same. The chaser now has its own set of angular rates and quaternions, and is subject to a modified version of Equation 2.4:

$$\dot{\omega}_C = J_C^{-1}({}^C r_{tp,C} \times {}^C A^{\mathcal{O}} \mathbf{T} - \boldsymbol{\omega} \times J_C \boldsymbol{\omega} + \boldsymbol{\tau}_c) \quad (2.14)$$

The torque $\boldsymbol{\tau}_c$ are attitude control torques when present. Equations (2.7) and (2.8) are modified to use the chaser attachment point positions and velocities:

$$\hat{e} = \frac{{}^{\mathcal{O}} r_{tp,T} - {}^{\mathcal{O}} r_{tp,C}}{\| {}^{\mathcal{O}} r_{tp,T} - {}^{\mathcal{O}} r_{tp,C} \|} \quad l = ({}^{\mathcal{O}} v_{tp,T} - {}^{\mathcal{O}} v_{tp,C}) \cdot \hat{e} \quad (2.15)$$

where ${}^{\mathcal{O}} v_{tp,T}$ and ${}^{\mathcal{O}} v_{tp,C}$ are the inertial velocities of the attachment points. The chaser body is modeled as a cube with uniform mass distribution and a side

length of s_c . Its moment of inertia is calculated as $J_C = \frac{1}{6} \text{diag}(m_C s_c^2, m_C s_c^2, m_C s_c^2)$.

2.3.1 Validation

While the model described in this section is not significantly different than that in Section 2.2, it is still prudent to validate it. Given the work performed in validating the previous model, the simulation results using *ode45* with relative tolerance 10^{-9} are considered the baseline. This comparison presents an issue as the chaser is a rigid body. To account for this, a procedure for setting the initial conditions of the rigid chaser is developed. The tether heading vector given $N = 0$ and the target attachment point in the inertial frame, calculated from the initial conditions in Table 2.2, are used to place the chaser attachment point such that an initial elongation or slackness of the tether is appropriately set. This is calculated using the equation

$${}^{\mathcal{O}}\mathbf{r}_{tp,C} = {}^{\mathcal{O}}\mathbf{r}_{tp,T} - \delta l_0 \hat{\mathbf{e}} \quad (2.16)$$

where δl_0 is the initial tether length. To place the chaser c.o.m., Equation (2.16) is slightly modified, first by replacing ${}^{\mathcal{O}}\mathbf{r}_{tp,C}$ on the left hand side with \mathbf{R}_C then ${}^{\mathcal{O}}\mathbf{r}_{tp,T}$ on the right with ${}^{\mathcal{O}}\mathbf{r}_{tp,C}$. The δl_0 is replaced with the half chaser side length s_c :

$$\mathbf{R}_C = {}^{\mathcal{O}}\mathbf{r}_{tp,C} - \frac{s_c}{2} \hat{\mathbf{e}} \quad (2.17)$$

Finally, the chaser pose is set by a rotation matrix built using $\hat{\mathbf{e}}$ and ${}^{\mathcal{O}}\mathbf{r}_{tp,C}$:

$${}^{\mathcal{O}}A_0^C = [\hat{\mathbf{e}}_1 | \hat{\mathbf{e}}_2 | \hat{\mathbf{e}}_3] \quad (2.18)$$

$$\hat{c}_1 = \hat{e} \quad (2.19)$$

$$\hat{c}_3 = \hat{c}_1 \times {}^{\mathcal{O}}\mathbf{r}_{tp,C} ||{}^{\mathcal{O}}\mathbf{r}_{tp,C}||^{-1} \quad (2.20)$$

$$\hat{c}_2 = \hat{c}_3 \times \hat{c}_1 \quad (2.21)$$

The chaser attitude quaternion is then extracted from the initial rotation matrix ${}^{\mathcal{O}}A_0^C$. This process aligns the chaser \hat{c}_1 axis with the tether heading vector and accurately sets the initial elongation. Due to the short distance on orbit between the chaser c.o.m. and the chaser attachment point, its velocity remains unchanged. The resulting initial conditions, calculated using a δl_0 and s_c of 0 m and 1 m, respectively, as well as the values from Table 2.2, are in Table 2.4. The system parameters for the simulation are in Table 2.5. Once again, the *ode45* solver with relative tolerance 10^{-9} is used for simulation. Equation (2.13) is again used as the metric for the chaser and target position error. The same open loop thrust from Equation (2.11) is applied to the rigid chaser's c.o.m. There is no chaser attitude control (i.e. τ_c) present for this simulation.

Table 2.4: Initial conditions for the rigid chaser model validation (Section 2.3).

Variable	Value
\mathbf{R}_C (m)	$[-6176010.87, -42079.190, 2973766.82]^T$
\mathbf{R}_T (m)	$[-6176020.96, -42080.997, 2973743.40]^T$
\mathbf{V}_C (m/s)	$[-2457.79535, -4404.28547, -5712.40584]^T$
\mathbf{V}_T (m/s)	$[-2457.76467, -4404.28338, -5712.420604]^T$
\mathbf{q}_C (-)	$[-0.551521076, 0.667700907, 0.471155309, 0.167369874]^T$
\mathbf{q}_T (-)	$[-0.85286853, 0.15038373, -0.08682409, 0.49240388]^T$
$\boldsymbol{\omega}_C$ (rad/s)	$[0, 0, 0]^T$
$\boldsymbol{\omega}_T$ (rad/s)	$[0, .05, 0]^T$

The RMSE between the two simulations- the *ode45* simulation with tolerance 10^{-9} from Section 2.2.3 and the rigid chaser simulation described above - are presented in Table 2.6. The chaser and target position errors indicate that

Table 2.5: System Parameters for the rigid chaser model.

Parameter	Value
Chaser Inertia Matrix J_C (kg-m ²)	diag(83.3, 83.3, 83.3)
Target Inertia Matrix J_T (kg-m ²)	diag(15000, 3000, 15000)
Chaser Attachment Point $\mathcal{C}r_{tp,C}$ (m)	[0.5, 0, 0] ^T
Target Attachment Point $\mathcal{T}r_{tp,T}$ (m)	[0, -0.875, 0] ^T
Chaser Mass m_C (kg)	500
Target Mass m_T (kg)	3000
Young's Modulus E (GPa)	60
Tether Area A (mm ²)	0.784
Tether Damping c (Ns/m)	16
Tether Natural Length l_t (m)	30

the simulations are quite similar. To further show the similarities, the elongation and alignment angles for both simulations are presented in Figure 2.5. The elongations are hardly distinguishable. However, the alignment angles show some significant deviation as time progresses. This is attributable to the differences between the tether end body dynamics in each simulation. Overall, the results of simulating the rigid chaser model using the given solver and relative tolerance prove this model to be accurate.

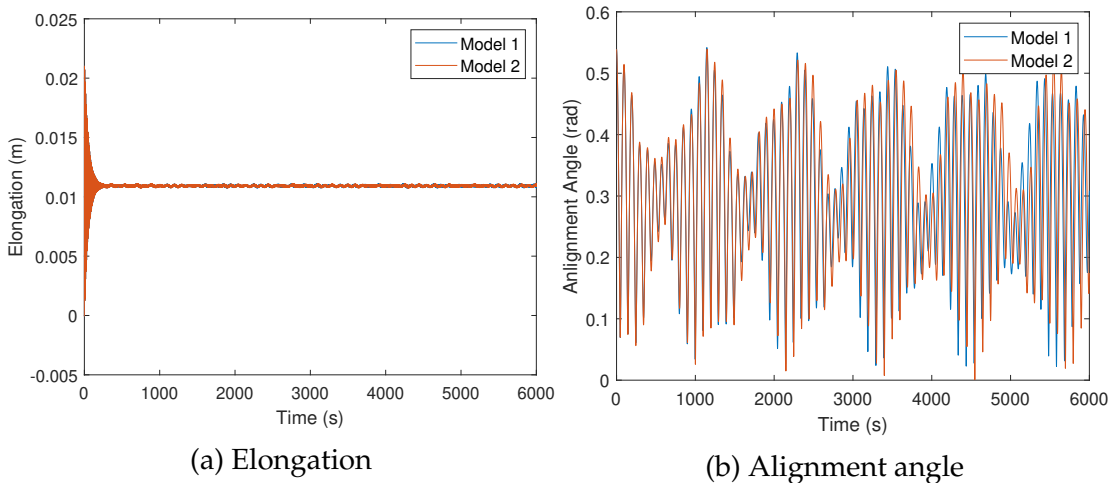


Figure 2.5: Simulation results with *ode45* and relative tolerance 10^{-9} . Model 1 and Model 2 are those described in Sections 2.2 and 2.3, respectively.

Table 2.6: RMSE between chaser and target positions of Model 1 and Model 2 simulations.

Chaser (m)	Target (m)
1.2812	0.8477

Chapter **3**

Impact of Tether Discretization on Target Attitude Motion

3.1 Introduction

Modeling of the dynamics of tethers in space is difficult and subject to uncertainties. It is therefore important to understand the impact that the tether model can have on the simulated system dynamics. This chapter presents results of modeling the tether with different numbers of nodes based on the model in Section 2.2. In particular, the effect the tether model has on the debris attitude motion is investigated.

3.2 Simulations

For testing the impact the tether discretization has on the target attitude motion, a total of 10 simulations were performed. These are grouped into two cases- 1 and 2- which differ based on their initial conditions. In case 1, the tether is

slightly tensioned initially (Table 2.2), and case 2 the tether is set with -3 m initial slackness. In both cases, one simulation is performed for each of the number of nodes: $N = [0, 2, 5, 7, 10]$. With $N = 0$, the tether is considered massless. The initial conditions of the chaser position for case 2 can be calculated using Equation (2.17), where the chaser attachment point position is replaced with its center of mass position and δl_0 is -3 m. The nodes' initial positions and velocities are calculated by linearly interpolating along the tether. For the n -th node:

$$\mathbf{R}_n = \mathbf{R}_C + \frac{n}{N+1} \left({}^O\mathbf{r}_{tp,T} - \mathbf{R}_C \right) \quad (3.1)$$

$$\mathbf{V}_n = \mathbf{V}_C + \frac{n}{N+1} \left({}^O\mathbf{v}_{tp,T} - \mathbf{V}_C \right) \quad (3.2)$$

The system parameters are in Table 2.1. The open loop thrust from Equation (2.11) is present with a magnitude of 20 N. It is shut off at 250 s to understand the tether motion given a failure of the chaser to regulate a relative distance. Each simulation is run for a total time of 500 s.

The results for case 1 are displayed in Figure 3.1. The elongation is calculated as the sum of the tether segment lengths l_i at each time step. As expected given the formulation of the tether model, the slightly tensioned tether produces similar elongation across N (Figure 3.1a). After 250 s, the elongations begin to differ, due to slight differences in velocity between the nodes. In fact, for $N > 0$ the segments do not uniformly become slack. The relative motion between the tether segment closest to the target and the target itself causes a small magnitude tension event. Due to the low mass of the nodes (on the order of 10^{-2} kg), the N -th node's motion is affected significantly more than the target's. This results in a chain of small tension events down the tether, which slowly brings each segment length to l_0 , causing the differences in the elongation. The time of

that first tension event is dependent on the segment length, and therefore N . In regards to the target angular rates in Figure 3.1b where ω_y is not plotted as its unchanging, the attitude motion of the debris is largely unaffected by N . The differences in the angular rates are insignificant. Additionally, the alignment angles show no significant differences while tension is maintained in the tether. However, the peak alignment angle after switch-off increases with N .

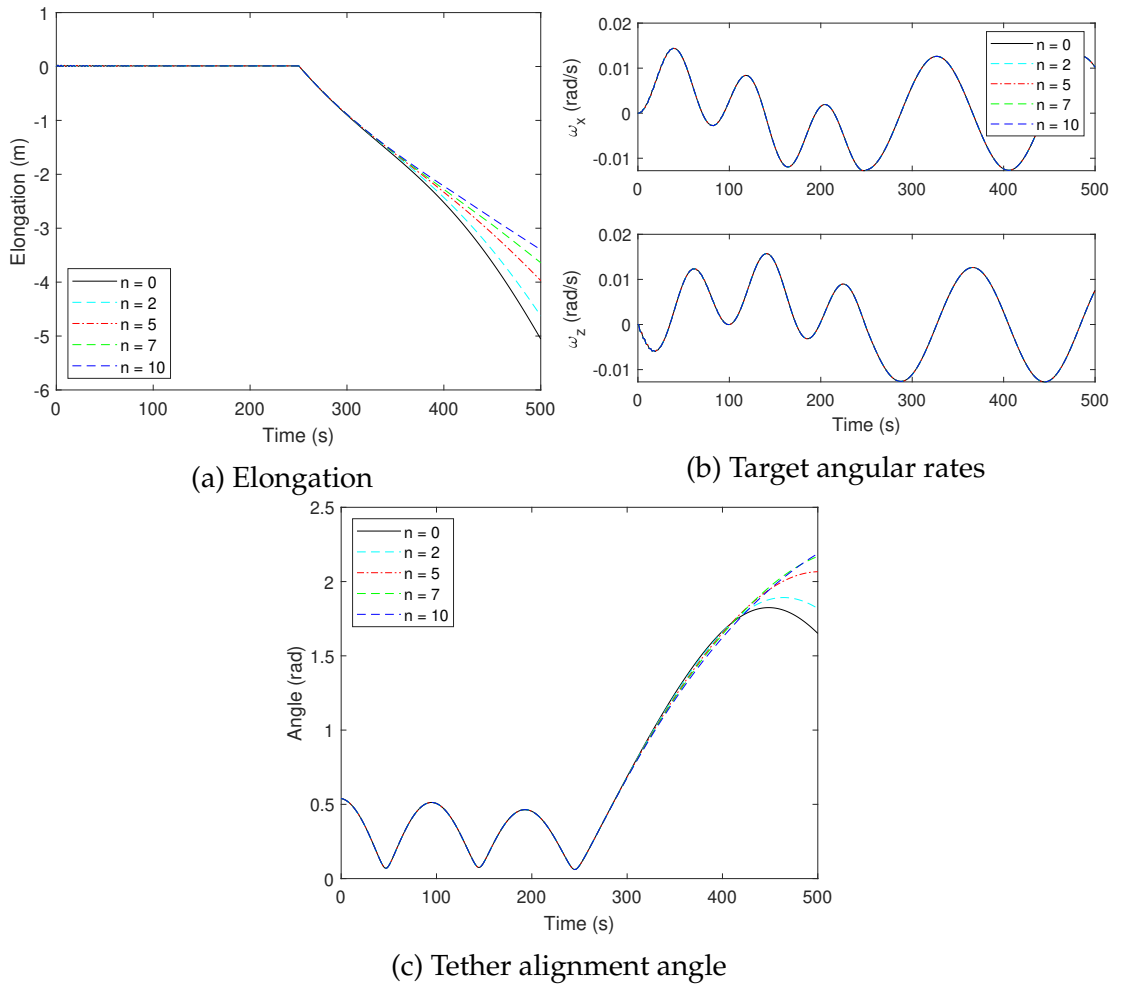


Figure 3.1: Results for case 1: tether slightly tensioned initially.

Figure 3.2 displays the results for case 2. The different system dynamics as a result of the initial conditions is readily apparent. The elongation in Figure 3.2a

displays interesting behavior. For $N = 0$, the tether clearly goes slack, while for $N > 0$ it is not evident the tether is going slack for $t > 50$ s. Figure 3.2b shows the center of mass distance between the chaser and target. It indicates that, along with the elongation behavior, the tether segments remain around l_0 while the end bodies approach each other. The transverse motion of the nodes causes this behavior, as motion off the nominal tether line - \hat{e}_0 - results in small tension events. To further illustrate this point, Figure 3.3 shows the system, including the target, chaser, nodes, and tether segments, at $t = 50$ s for all N . The transverse behavior is clear for $N > 0$. The small tension events, driven by the node motion as opposed to the chaser-target relative motion, are visible in the segments. The slack-taut behavior present in the tether poses an issue due to the large tensions developed in the tether, as well the inability to control the debris when slack. Additionally, these images provide a better understanding of the alignment angles in Figure 3.2d. The transverse tether motion causes a significant difference in the motion of node N between the simulations, resulting in the seemingly erratic behavior of the alignment angle for $t < 250$ s. The disparate behavior of the alignment angles after $t = 250$ s is also due to the node motion. It should be noted that all the alignment angles indicate some degree of collision between tether and target. The angular rates in Figure 3.2c begin to drift at around 90 s, which corresponds to the fourth tension event. This drift is associated with the changing rate at which the tether becomes tensioned, most easily visible in Figure 3.2b where the peaks indicate a tension event. The center of mass distance also provides an explanation for the angular rate behavior when $t > 450$ s. Slight variations of the chaser-target relative positions and velocities when the burn cuts off results in different times at which they pass each other, ultimately causing the sudden target angular rate spikes once the tether

is tensioned again.

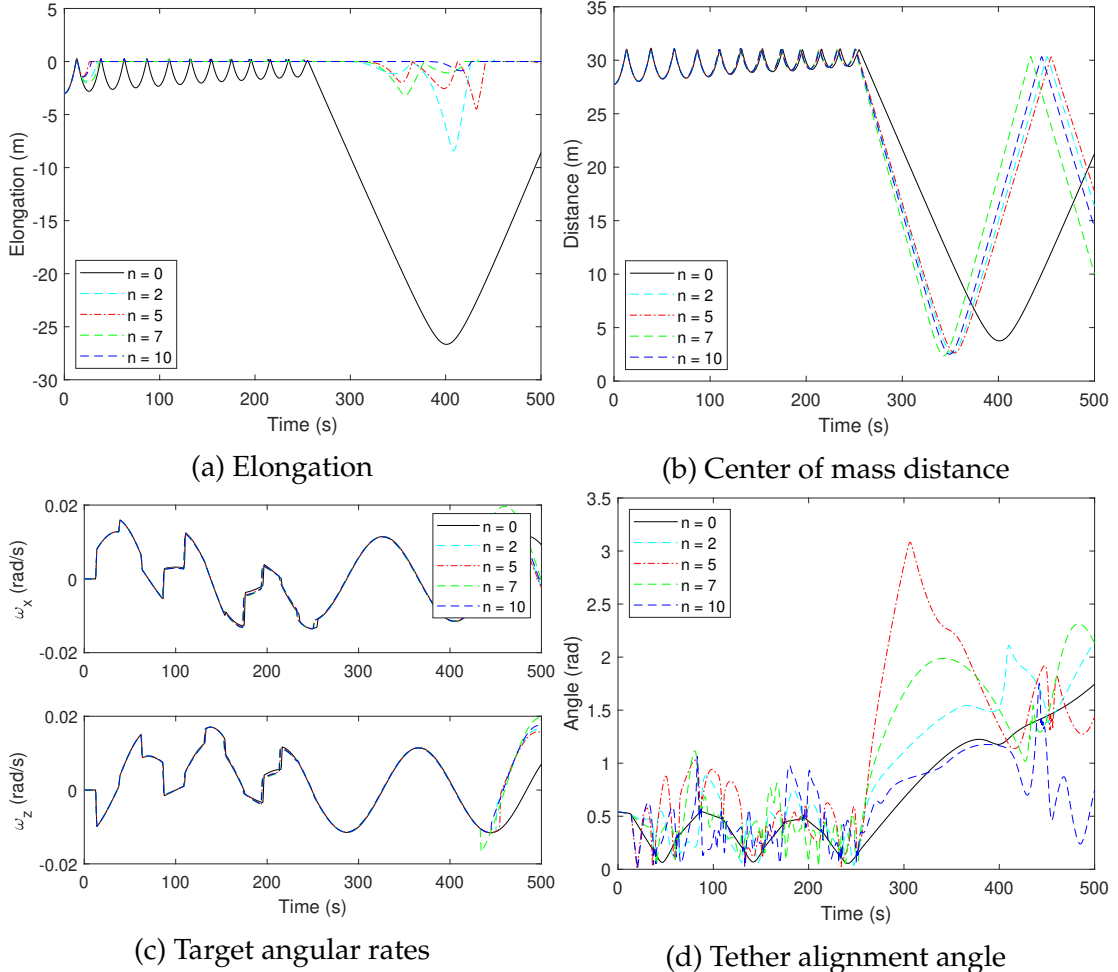


Figure 3.2: Results for case 2: tether -1 m slack initially

These results indicate that the target attitude motion is negligibly affected by the discretization of the tether while the system is controlled. However, with more violent system dynamics, represented here in case 2, the uncontrolled (i.e. post-burn) system behavior shows some variability in the timing and magnitude of key events. Specifically when an alignment angle greater than $\frac{\pi}{2}\text{ rad}$ occurs and the minimum chaser-target distance is reached. As these are both measures of mission safety, its prudent to simulate an ADR scenario with differ-

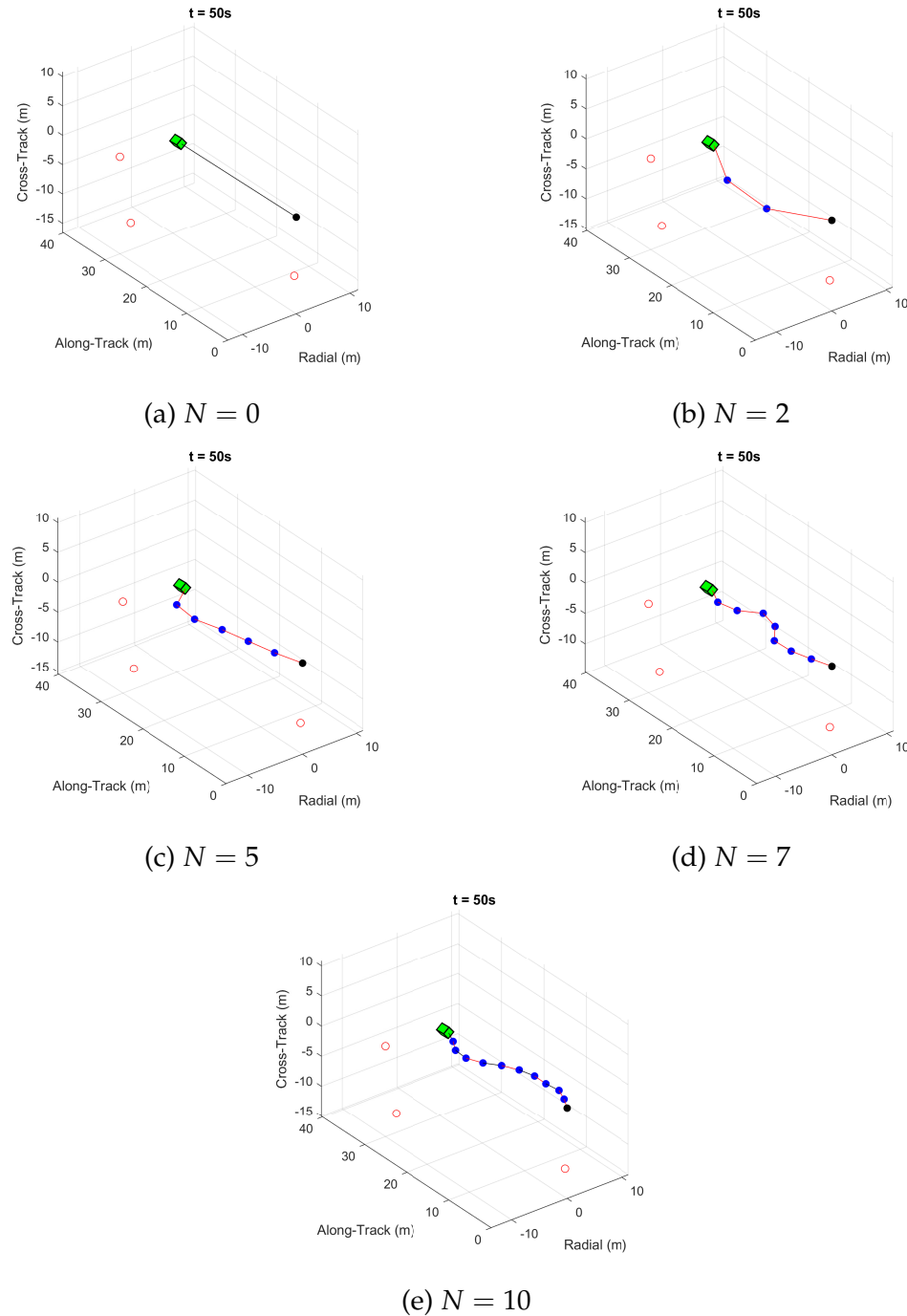


Figure 3.3: Image of system at $t = 50$ s in the chaser LVLH frame. The target is green, the chaser black, and the nodes blue. The lines connecting these are the tether segments, shown in two colors: red for tensioned and black for slack.

ent N if tether winding or a possible collision is suspected. Even still, simulation with $N = 0$ is sufficient to display the overall system behavior for the given scenarios.

Chaser Controls

4.1 Introduction

Control of the chaser craft is required to perform all tasks in the ADR mission. Correctly orientating the chaser is necessary to prevent tether winding and other deleterious events from occurring during the removal mission, as well as pointing the chaser's thrusters appropriately. In the previous chapters, a distance between the chaser and target was maintained using an open loop controller. However, it was shown that it can cause unwanted cycles of slackness and tautness in the tether. Here, an attitude controller for the chaser is discussed in the context of the ADR scenario. Then, a relative distance PID controller is designed and its merits compared to the open loop controller from Section 2.2.3.

4.2 Chaser Attitude Control

Spacecraft attitude control is a well developed field. With this being true, and the primary investigations of this work relating to the tether modeling and at-

titude motion of the target, an existing attitude controller for the chaser was implemented. The sliding mode controller designed by Crassidis et al. [44] was shown to be effective in controlling a satellites attitude, and, for this reason, chosen to be implemented. The controller will be briefly discussed before displaying its performance in the context of the tethered satellites.

The error quaternion, which represents the misalignment between the desired and actual attitude, is calculated as

$$\mathbf{q}_e = Q(\mathbf{q}_d)^T \mathbf{q} \quad (4.1)$$

$$q_{es} = \mathbf{q}^T \mathbf{q}_d \quad (4.2)$$

where \mathbf{q}_d is the desired quaternion, $Q(\mathbf{q}_d)$ is the matrix $Q(\mathbf{q})$ in Equation 2.14 populated with \mathbf{q}_d , \mathbf{q}_e is the error quaternion vector components, and q_{es} the scalar of the error quaternion. The sliding manifold, s , chosen in [44] is

$$s = (\boldsymbol{\omega} - \boldsymbol{\omega}_d) + K \text{sgn}(q_{es}) \mathbf{q}_e \quad (4.3)$$

with $\boldsymbol{\omega}_d$ as the desired angular rate and K a positive constant. As reaction wheels are not considered in the relevant model described in Section 2.3, the external torque control equation was implemented:

$$\begin{aligned} \tau_c = & \boldsymbol{\omega} \times J_C \boldsymbol{\omega} + \\ & J_C \left(\frac{1}{2} K \text{sgn}(q_{es}) (Q(\mathbf{q})^T Q(\mathbf{q}_d) \boldsymbol{\omega}_d - Q(\mathbf{q}_d)^T Q(\mathbf{q}) \boldsymbol{\omega}) + \dot{\boldsymbol{\omega}}_d - G \text{sat}(s, \epsilon) \right) \end{aligned} \quad (4.4)$$

where $\text{sat}(\cdot, \epsilon)$ is the saturation function, ϵ is a tunable parameter defining the boundary layer width, and G is a positive definite gain matrix.

In the context of the tethered satellite scenario, the objective of the controller

is to point \hat{c}_1 along the tether (Equation (2.7) with $N = 0$) to reduce the possibility of tangling. To point the chaser in the correct direction, a set of desired axes is defined using \hat{e} as the x -axis. The z -axis is then the cross product of \hat{e} and R_C , and the y -axis completes the right-handed set. A rotation matrix is constructed from this set, and the desired attitude quaternion is extracted from this matrix.

To test the implementation of this controller, a simulation of the model in Section 2.3 is performed for a total simulation time of 6000 s. The sliding mode control parameters are $K = 4$, $G = \text{diag}(1, 1, 1)$, and $\epsilon = .001$. The 20 N open loop thrust is active throughout the simulation. The chaser frame C is initially slightly misaligned with the desired axes and the tether is slightly tensioned (conditions from Table 2.4).

Figure 4.1 displays the results. The controller responds to the initial misalignment event, as is indicated by the large peak in Figure 4.1b. After this, the control torques oscillate with small amplitude around 0 Nm. The angular rates of the chaser in Figure 4.1a, while not completely damped, are steady and pose no threat to tangling. This is evident in the chaser alignment angle in Figure 4.1d, which is far below the $\frac{\pi}{2}$ rad winding limit. The controller is clearly effective at maintaining the correct pose of the chaser. While the gains could be reduced to produce a less taxing control response, they are considered sufficient for the purposes of this work. This controller and the chosen gains are present in all of the simulations following this section.

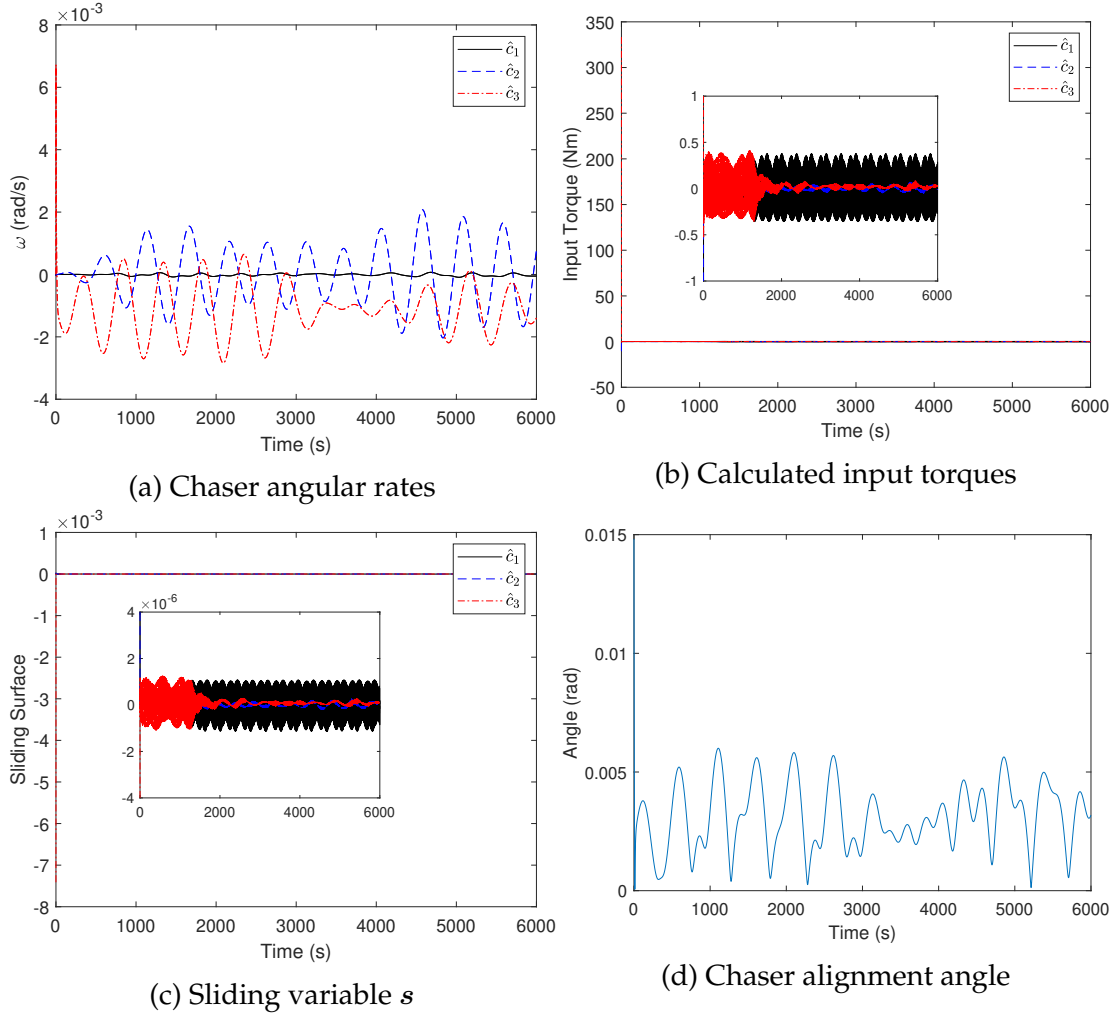


Figure 4.1: Sliding mode control results.

4.3 Relative Distance PID Control

The results of using an open loop controller displayed significant oscillation in the tether elongation (Section 3.2, Figure 3.2a), behavior which can be deleterious given a failure of thrust or if the tether disconnects from the target as collision chances increase significantly. These results also showed that the torque from the tether can easily induce angular motion of the target. Therefore, developing a control which can reduce the induced angular motion while main-

taining a set distance from the target is a net positive on the safety of the target removal mission.

For the purpose of investigating if controlling the tether length can reduce the induced angular motion on the target, a PID controller was developed which controls the relative distance between the tether attachment points on the chaser and target. This essentially regulates the elongation such that there is a slight residual tension to ensure safety by maintaining a relative distance. The actuators considered are the main thrusters of the chaser craft. Thrusting is assumed to be continuous and exactly able to track the required input calculated by the control. Information regarding the target, including its position and velocity relative to the chaser, its orientation and angular velocity, as well as the attachment point of the tether on the target, is assumed to be readily available. The process variable for this control is

$$e = \Delta l + l_0 - l \quad (4.5)$$

where Δl is the desired elongation. The derivative of the process variable is simply $-\dot{l}$ (see Equation 2.15). Choice of Δl ultimately impacts the fuel consumption and angular momentum imparted to the target, and should therefore be as small as possible. The input magnitude calculated using this process variable is

$$F_{PID} = K_P e + K_I \int_0^t e dt + K_D \dot{e} \quad (4.6)$$

The proportional, integral, and derivative gains are K_P , K_I , and K_D , respectively. Finally, this calculated thrust is fired along the tether heading direction to di-

rectly counteract the tether motion:

$$\mathbf{F}_{PID} = -F_{PID}\hat{\mathbf{e}} \quad (4.7)$$

Due to the choice of $\hat{\mathbf{e}}$, a positive F_{PID} indicates that the chaser is thrusting away from the target. The thrust \mathbf{F}_{PID} is applied directly to the chaser center of mass. The gain tuning procedure is discussed in the following section.

4.3.1 Tuning of PID Gains

Tuning of the PID gains was performed heuristically. Each of the gains was varied over a range of values, while the other two were set as constants. To test the performance of the varying gain, simulations were run for δl_0 of -0.03 m (initial conditions calculated as described in Section 2.3.1). A desired elongation of 0.01 m was chosen, as this is around the steady state of the 20 N open loop controller, providing a basis for comparison. The base gains, the ones which are not varying for a given set of simulations, are $K_p = 200$ N/m, $K_i = 20$ N/ms, and $K_d = 500$ Ns/m. The chaser attitude controller is active during this simulation. The final gains were chosen based on their performance in controlling the elongation, regardless of target attitude motion.

Figure 4.2 includes the elongation and control inputs for variations of the gains with an initial slack in the tether. Of course, increasing K_p (Figure 4.2a) causes a larger peak elongation, and therefore tension. The transient is less affected by an increase in K_i than K_p (Figure 4.2c). However, an increase in K_i is beneficial for the settling time, which is decreasing. The gain K_d has the largest impact on the transient behavior, as it is effectively increasing the damping of the system, reducing the oscillations and overshoot of the elongation. Based on

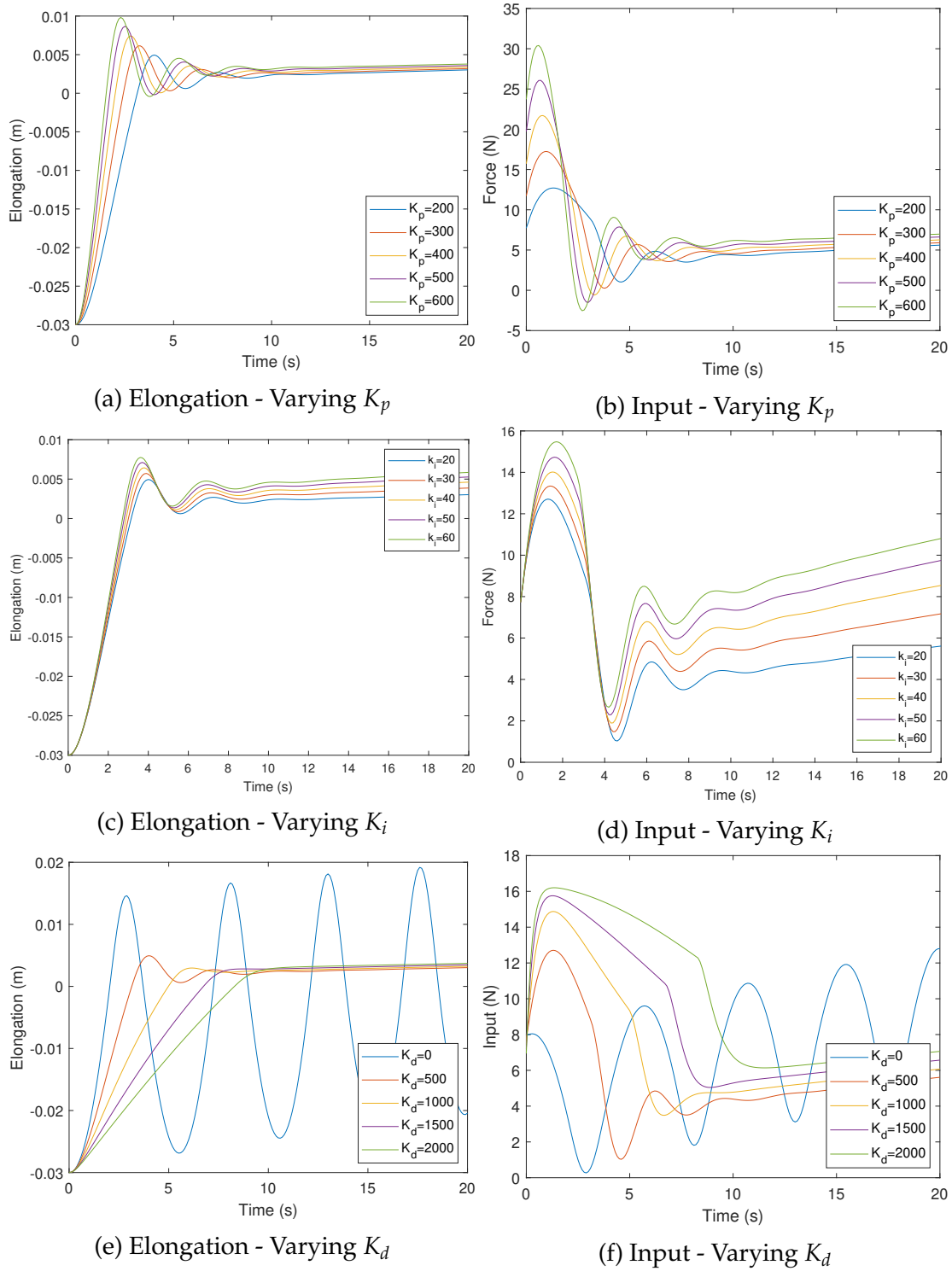


Figure 4.2: Negative initial elongation with varying gains.

these plots, gains of $K_p = 300 \text{ N/m}$, $K_i = 300 \text{ N/ms}$, and $K_d = 2000 \text{ Ns/m}$ were chosen. The K_p choice was made based on the speed of the response and the peak elongation, which should be limited where possible. The nearly critically damped behavior present when K_d is large is beneficial, limiting the resulting peak elongation. While not a part of the variations, the choice of K_i is derived from the impact it has on the settling time. This will increase the peak elongation, but was considered worthwhile for the settling time reduction.

4.3.2 Comparison of PID and Open Loop Performance

To gauge the performance of the PID controller, it is directly compared to the 20 N open loop thrust given the same initial conditions and system parameters. Four simulations were run total: two for the PID and two for the open loop control. Both controls are utilized for initial elongations of -1 m and 0.01 m , which represent different post-capture scenarios – the latter elongation is at the desired value Δl . The system parameters are the same as in Table 2.5. Due to the choice of $\tau_{r_{tp,T}}$, the target angular rate ω_y is not plotted in either case. The initial conditions are again calculated from the procedure in Section 2.3.1.

The results of the negative initial elongation (i.e., -1 m) simulations are in Figure 4.3. The PID controller is very effective in regulating the tether elongation, and therefore the tension (Figure 4.3a and 4.3b). The desired elongation is reached in about 50 s, while the open loop control elongation continues to oscillate with large periods of slack until 450 s, after which the tether is no longer slack (this is more visible in 4.3b). Compared to the open loop controller, the PID has about double the elongation peak, caused by the large control thrust in Figure 4.3e. This results in a significantly greater moment applied to the target in

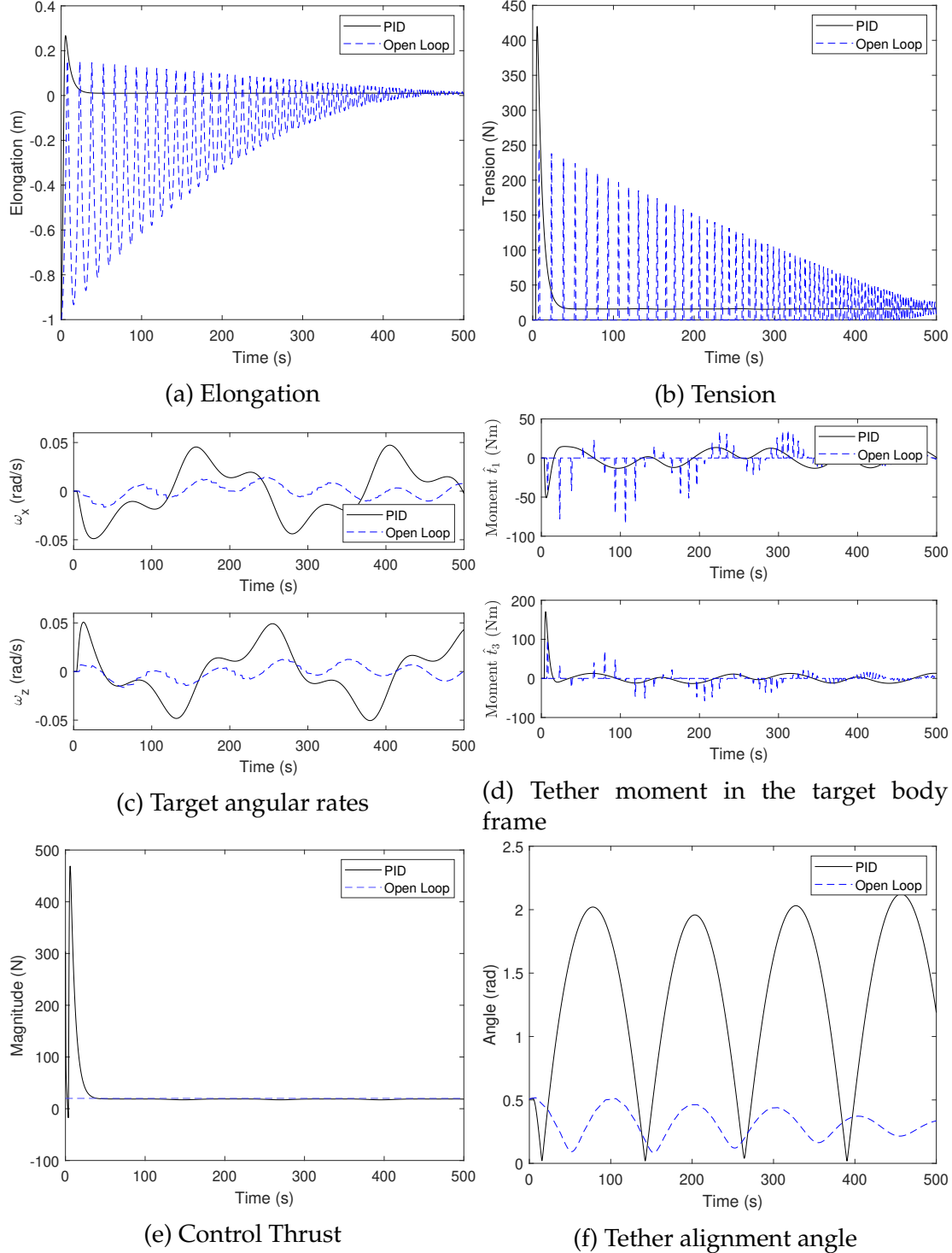


Figure 4.3: Results comparison of PID and open loop for 1 m initial slack.

the first 50 s of the simulation (Figure 4.3d), inducing the larger angular rates in Figure 4.3c. In fact, as can be seen in Figs. 4.3f and 4.3c, the open loop controller has a much slighter impact on the target attitude motion than the PID controller for the initial slack tension case. The alignment angle behavior for the open loop controller is the same as seen in Figure 2.2b, while the PID controller induced a dangerous tumbling behavior (the alignment angle peaks above $\frac{\pi}{2}$ rad). This is a direct result of the large initial tension generated by the PID thrusting.

Figure 4.4 displays the results for 0.01 m initial elongation. The PID controller is able to command the elongation to the desired value in 25 s with zero overshoot, indicating a superior performance than the open loop by this metric (Figure 4.4a). The elongation does drop below the desired due to the initial tension and required response from the control. The impact on the target attitude motion is considerably more similar than for the negative initial elongation simulations. In Figure 4.4c, it can be seen that the target angular rates have the same behavior between the two controllers. However, Figure 4.4f shows the different behavior in the alignment angle persisting. The open loop has nearly the exact same alignment angle behavior as in Figure 4.3f. This must be a result of the difference in the thrusting direction of the two controllers, where the off tether heading direction thrusting of the open loop results in the oscillatory behavior of the peak alignment angle magnitude.

It is clear from these simulations that the PID controller is successful in regulating the relative distance between the attachment points. The potentially dangerous attitude behavior the PID induces, given a significant initial slackness in the tether, limits its safe use to when the tether is either slightly slack or pre-tensioned. It could remain in its current form as part of a larger control strategy, but must be significantly modified to account for the target angular

motion in order to ensure safety and robustness to initial conditions.

4.3.3 Saturation of Control Input

Actuator limitations must be taken into account for the application of control strategies to real missions. As the PID controller utilizes the chaser craft's thrusters, the most relevant limitation is the maximum thrust that can be generated. The nature of the mission requires that the chaser's primary engines face along the tether direction towards the target, indicating an asymmetric thrust capability in this direction. This asymmetry is simulated by setting upper and lower limits on the magnitude of F_{PID} (Eq. 4.6). As stated in the previous sections, a positive F_{PID} is thrusting away from the target, and will therefore have a larger saturation limit. A lower saturation limit will be in the opposite direction, representing the chaser's reaction control system thrusting capabilities. Three upper saturation limits were tested, all with the same lower saturation limit of -50 N . In order to see the effects of the saturation, an initial slack in the tether of -3 m is set ($\delta l_0 = -3\text{ m}$). Anti-windup of the integrator is implemented using clamping, as this is compatible with the *ode45* solver. The results of these simulations using the system parameters in 2.5 are in Figure 4.5.

In Figure 4.5e, it is clear that the 500 and 1000 N saturation limits are reached. The 2000 N saturation limit was not reached, but was included to compare the saturated and unsaturated system responses. While the calculated control input is larger than the limit, the PID essentially acts as an open loop thrust. The effects of this are most easily visible in the elongation, Figure 4.5a. For the 1000 N saturation, the open loop behavior is ended in about 21 s. Once the saturation limit is reached, the integrator clamping takes effect. As the initial drivers of

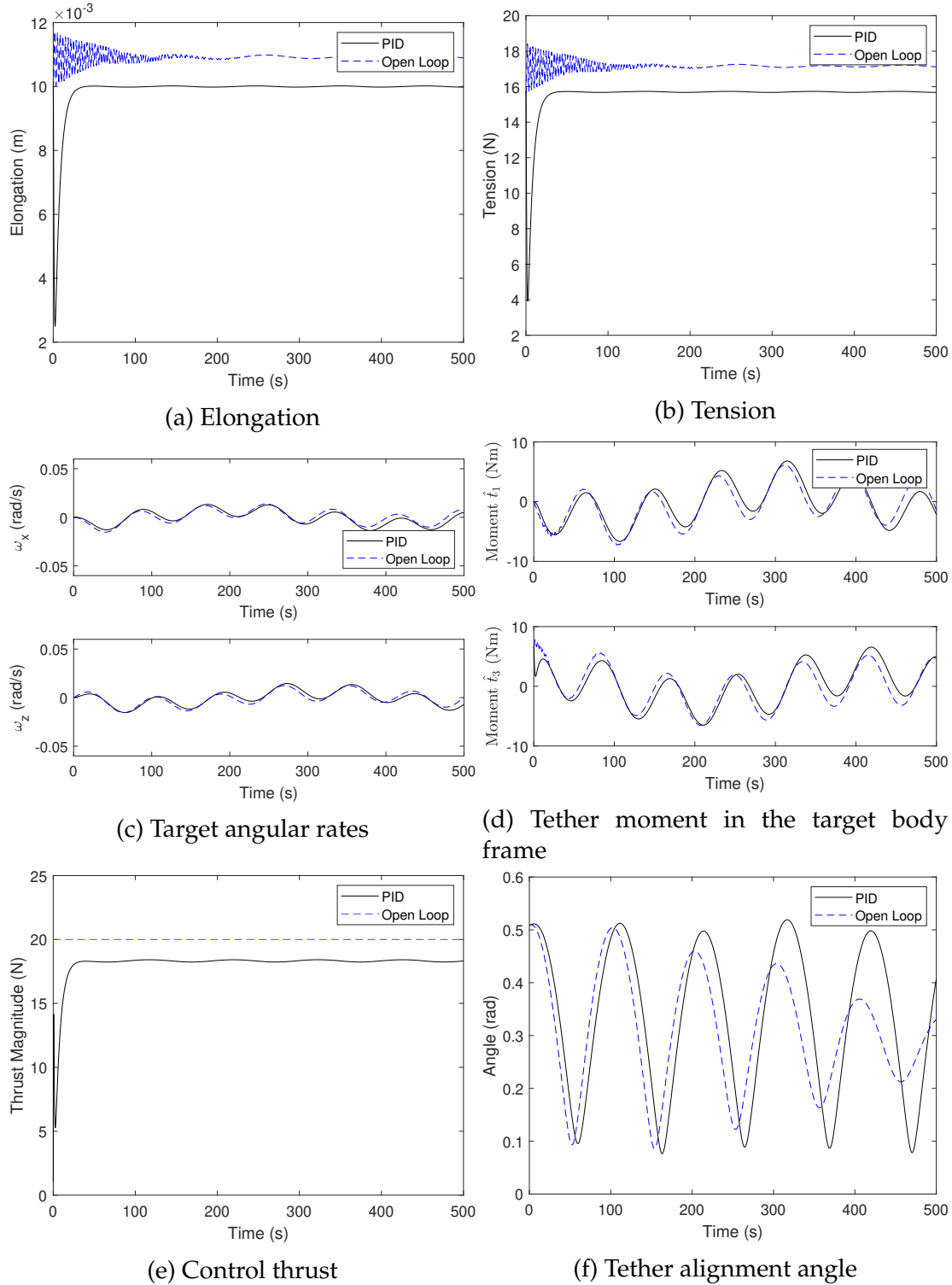


Figure 4.4: Results comparison of PID and open loop for 0.01 m initial slack.

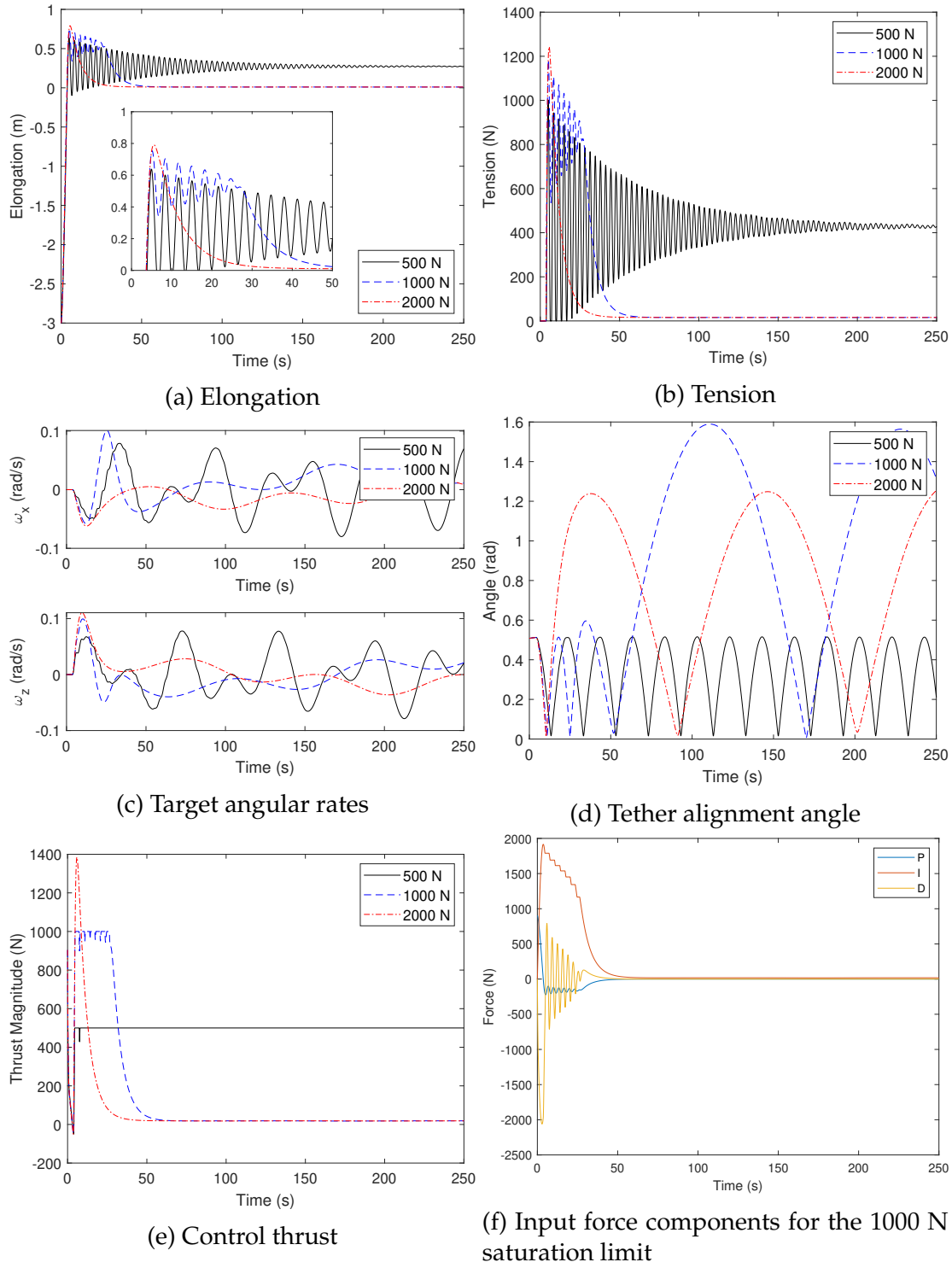


Figure 4.5: Results for different saturation levels.

the large magnitude of the control are the derivative and integral components (Figure 4.5f), the error integral, and therefore its associated force, remains large. This error integral is slowly reduced, as the negative peaks of the derivative component are enough to reduce the total calculated input below the saturation limit. The situation for the 500 N saturation limit is significantly different: it remains an open loop controller throughout the entire simulation. Considering the first 4 seconds for each limit is nearly the same, the issue becomes apparent after the tether is taut. The lower the saturation limit, the less responsive the controller can be to the tension force generated by the pre-tension thrusting of the chaser. This is evident in the ratios of the maximum tension to the maximum applied input force, which are 2.002, 1.186, and 0.895 for the 500 N, 1000 N, and 2000 N limits, respectively. As a result of this, the effects of the initial tension dominate the elongation dynamics, which, combined with the lower saturation limit and about the same integral error peak as the higher limits (due to the slack dynamics), results in the inability of the derivative and proportional components to cancel the integral component of the PID controller with the 500 N limit.

The target attitude dynamics display interesting behavior across the saturation limits. Firstly, Figure 4.5c shows that ω_x and ω_z are consistently the largest for the 500 N saturation limit. This is counter-intuitive to the previous results shown in Figure 4.3c, where the greater initial tension of the PID resulted in consistently greater angular rates compared to the open loop. This can be explained by the applied moment on the target, which remains large for an extended period of time compared to the other saturation limits (see Figure 4.6a). An interesting result of this is in the alignment angle (see Figure 4.5d). The 500 N limit has the smallest peak alignment angle, as well as the highest frequency oscilla-

tions. The 1000 N limit behaves the same until the tension is relaxed at about 26.3 s. As the peak tensions are roughly the same, the explanation for this behavior must lay in the applied moment. When the saturation limit is exceeded, the tension moment is the largest contributor to the angular acceleration, essentially dictating the angular motion of the target. This is visible in Figures 4.6a-4.6d. However, upon relaxing the tension, this is no longer the case. The contributions to the angular acceleration from the fictitious moment ($\omega \times J_T \omega$ in Equation 2.4) and the tension result in slow, steady sinusoids (see Figs. 4.6d and 4.6f). The 500 N limit never leaves the saturated control regime once in it, meaning the applied moment remains large, while the lower frequency, large amplitude alignment angle behavior present in both the larger limits is indicative of the tether relaxation. The 1000 N limit causes the largest alignment angle, with a peak above $\frac{\pi}{2}$ rad, as it applies a greater maximum moment than the 2000 N limit.

This analysis shows that the saturation of the control can result in potentially dangerous scenarios, particularly for the 1000 N limit, where contact between the tether and target would have occurred. With clamping implemented as the anti-windup, it is possible that the control does not return to the unsaturated regime. Given this, it would be necessary to tune the gains taking the saturation limits into account. An interesting conclusion of this work is that the moment applied by the tether should have a consistent peak amplitude to maintain a small amplitude of the alignment angle. A large difference between the peak and steady-state tensions results in unfavorably large alignment angles. This was evident in the 1000 N and unsaturated responses, where the angular momentum change induced by the initial applied moment is not countered by moments of similar magnitude after the tension relaxes. The current controller, as

well as future controller designs, can be improved by leveraging this knowledge.

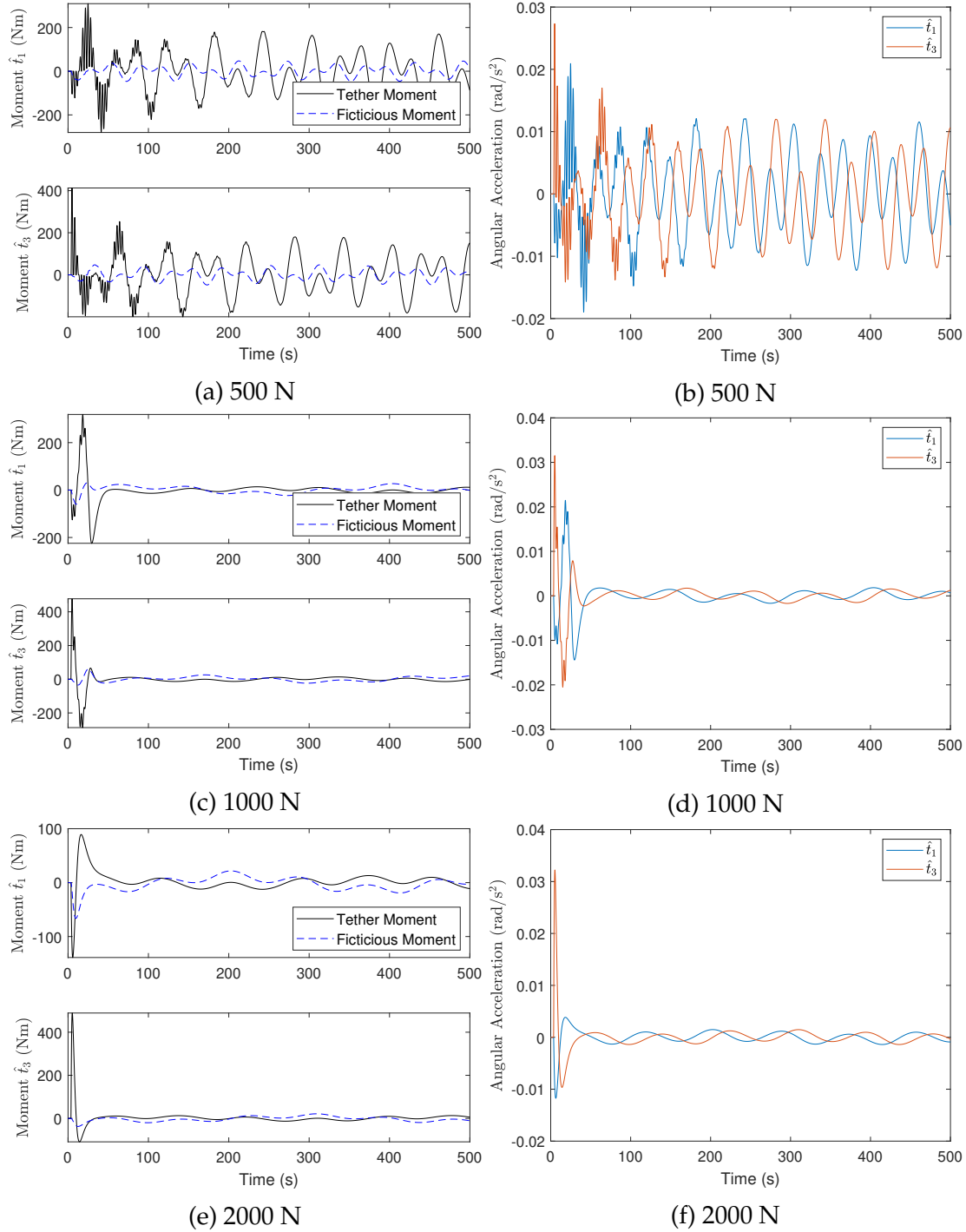


Figure 4.6: Target applied moment and angular acceleration for different saturation levels.

Chapter **5**

Vortex-Studio-Based Simulator

Validation

5.1 Introduction

While most works ignore modeling of the net in the post-capture scenario [11, 16, 26, 45], its inclusion will provide a greater understanding of the dynamics and control of tethered-net removal systems after capture of debris. Botta et al. developed a tethered-net capture simulator using a commercial simulation framework, Vortex Dynamics (now Vortex Studio), developed by CM Labs [11, 13, 16, 28]. In those works, gravitational acceleration was ignored due to the short duration dynamics of the deployment and capture phases (of less than 2 minutes). However, in the considerably longer post-capture phases, a zero gravity environment is not representative of the complex system dynamics on orbit. By including gravity in the net simulation, the post-capture dynamics can be analyzed, the influence of the net during detumbling and deorbiting can be investigated, and controls developed using the reduced models of Chapter 2

can be validated. This chapter briefly introduces the Vortex Studio engine; then, the results of simulating the model in Section 2.3 are compared to those of the same model in MATLAB for validation.

5.2 Vortex Studio Engine

Vortex Studio is a commercial multibody dynamics engine allowing for user-defined system simulation and visualization. A system can be implemented by defining rigid bodies, known as *parts* in the software, and connecting them with various kinematic constraints. In the context of the ADR scenario, the tether can be modeled using a *distance joint*, which is a positional constraint of the form

$$\|\mathbf{R}_2 - \mathbf{R}_1\| - d \leq 0 \quad (5.1)$$

where d is the maximum allowable distance between the positions \mathbf{R}_1 and \mathbf{R}_2 . These positions are the attachment points of the joint on two rigid bodies. For simulating the system, they are the tether attachment points on the chaser and target such that the resultant is the elongation $l - l_0$. This constraint can be relaxed using a spring-damper for when $\|\mathbf{R}_2 - \mathbf{R}_1\| - d > 0$ such that the following equation holds:

$$\mathbf{T} = \begin{cases} T\hat{\mathbf{e}} & \text{if } (l > l_0), \\ 0 & \text{if } (l \leq l_0) \end{cases} \quad (5.2)$$

The tension T is the same as calculated in Equation (2.6). However, there is a distinct difference between this equation and Equation (2.6), in that there is no check for the tension force being positive. This modeling difference for

the tension has been validated for net deployment and debris capture by Botta in [16]. Once the bodies and constraints have been defined, Vortex organizes the resulting dynamics and constraint equations into a linear complementarity problem. This is solved with a semi-implicit discrete-time integrator, which uses the positions at the current time step and the velocities at the next time step (see [16] for more details).

While the Vortex engine can handle complex constraints and rigid body dynamics, the standard implementation of gravity is limited to a constant value throughout the simulation. It is set at the highest level of the simulation hierarchy as a single vector quantity in units of acceleration (m/s^2). This is effective for many of the ground-based simulation applications that Vortex Studio is used for, but causes an issue for the simulation of an on-orbit ADR scenario. Therefore, position-dependent gravitational acceleration had to be implemented through the addition of external forces to the parts in the simulation. This was implemented via the Vortex SDK interface in C++, which allows for greater freedom in creating user-defined simulations. As for the model in Section 2.3, Newtonian gravity is used and directly applied to each part:

$$\mathbf{F}_G = -m\mu \frac{\mathbf{R}}{||\mathbf{R}||^3} \quad (5.3)$$

where \mathbf{R} is the part's inertial position.

5.3 Validation

To validate the implementation of Newtonian gravity in the Vortex engine, the same model as in Section 2.3 is constructed using parts for the chaser and tar-

get, with a relaxed distance joint as the tether. The distance joint is attached to the surface of the chaser and target at the attachment points given in Table 2.5. An image of the system in Vortex showing the end bodies and the distance joint is in Figure 5.1. The Vortex-Dynamics-based results are compared to those of MATLAB for the same initial conditions and system parameters. The parameters are the same as in Table 2.5, except that the target inertia is changed to $J_T = \text{diag}(1156.25, 781.25, 1156.25)$ kgm². The initial conditions are for the slightly tensioned tether in Table 2.4, with $N = 0$. The open loop and sliding mode controllers are both present on the chaser, with $F_{OL} = 20$ N. The total simulation run time is 1000 s. The internal time step for the Vortex integrator was set to 0.0001 s.

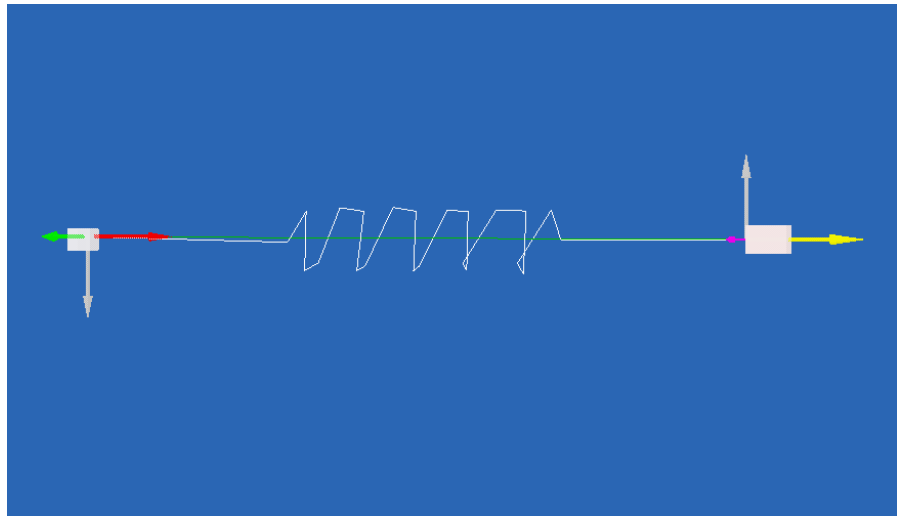


Figure 5.1: System in Vortex with chaser on the left, target on the right, and distance joint connecting them. The axes at either end of the joint are its attachment point axes.

The RMSE of the positions, velocities, and angular rates of the chaser and target between the simulations, taking the MATLAB simulation as the truth, are presented in Table 5.1. The chaser and target position and velocity errors are on the order of 10^{-1} m and 10^{-4} m/s, respectively. These errors indicate a high de-

gree of accuracy between the simulations. Considering that the inertial position components of the bodies are on the order of 10^6 m, the positional accuracy indicates an effective Newtonian gravity implementation. The deviations are likely the result of the different integrators. Additionally, the small error in the chaser angular velocities means the sliding mode controller was successfully implemented. The accuracy of the relative motion of the bodies is displayed through the elongation and center of mass distance in Figure 5.2. The nearly identical results further indicate that the improved Vortex-Dynamics-based simulator is suitable for representing the post-capture tethered ADR scenario on orbit.

Table 5.1: RMSE with respect to baseline simulation.

Body	Position (m)	Velocity (m/s)	Angular Rate (rad/s)
Chaser	0.291365	$9.55097 \cdot 10^{-4}$	$6.84185 \cdot 10^{-7}$
Target	0.291362	$9.54841 \cdot 10^{-4}$	$37.6461 \cdot 10^{-7}$

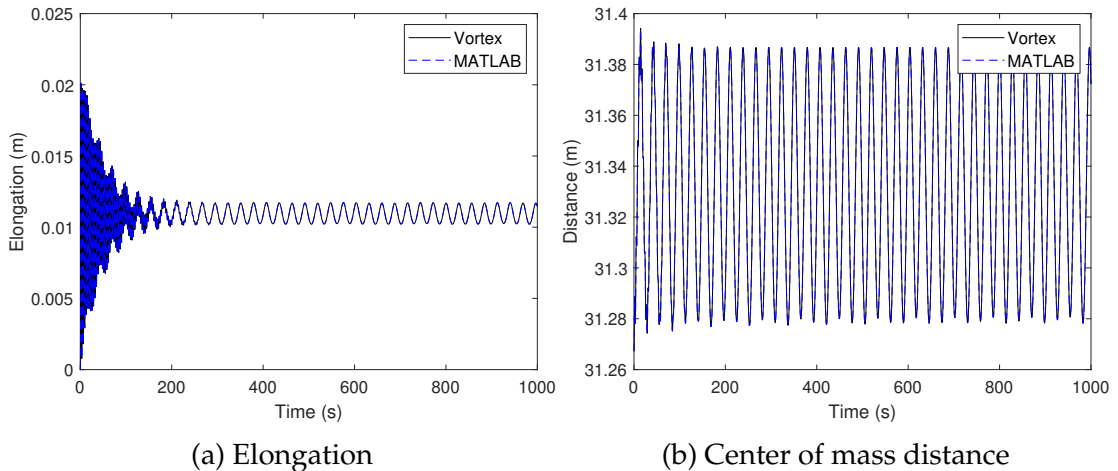


Figure 5.2: Vortex and MATLAB simulation results of the model in Section 2.3.

Conclusion

The dynamics and control of a tether-based active debris removal scenario in the post-capture phases was investigated in this work. For this purpose, two models were used for generating results of the system. The first model – consisting of a point chaser, a discretized tether, and a rigid target – was validated against results in the literature. Moreover, it was used to understand the effects of tether modeling using lumped parameters on the target attitude motion and chaser-target relative dynamics. The system showed very similar behavior, independent of the number of lumped masses under the influence of a constant thrust and in the presence of a taut tether. However, an initially slack tether produced differences in the degree of tether winding and minimum chaser-target relative distance after the thrust was shut off. Overall, the massless tether model (with no inner nodes) sufficiently displayed the overall system behavior. It is recommended to use lumped masses if winding or a collision is possible in a given ADR scenario.

The second model, which includes a rigid chaser, was used for increasing fitness to reality and for implementing chaser controls. The sliding mode atti-

tude controller designed by Crassidis et al. [44] was sufficient in aligning the chaser with the tether. A relative distance PID controller was developed, which was designed to maintain a constant length in the tether. The dynamics of the system under this controller was compared to that under constant thrust. While succeeding in controlling the tether length and therefore maintaining a tension in the tether, it failed to limit the induced angular motion on the debris. Effects of control saturation on the system dynamics were also investigated, and it was found that that a consistent tension in the tether kept the alignment angle magnitude at safe levels. While not achieving all of its goals, the implementation of this controller illuminated important system dynamics which can be leveraged in future control developments.

The future of this research lays in the inclusion of the net for post-capture dynamics simulations. A necessary component of simulating those dynamics is gravitation. A tether-net ADR simulator for the capture phase, in the absence of gravity, was already built in the Vortex-Studio engine in previous work. For simulating the post-capture dynamics, it was however necessary to validate inclusion of position-dependent gravity of the chaser and target. The second model described in this work was used to validate the on orbit ADR scenario in the Vortex-Studio-based simulator, by comparing its results to those produced by MATLAB. The results proved to match well, paving the way for developing the tethered-net post-capture simulator. It is expected that the presence of the net will help with debris detumbling. Moreover, with this simulator completed, further development and design of control systems can occur. It will also be useful for target state and parameter estimation purposes, as it will provide further information on the way the net affects the target debris motion. An unexplored aspect of the tethered-net removal system is way the flexible appendages inter-

act with the net during towing or reentry, which can be investigated using the improved simulator.

Bibliography

- [1] J-C Liou and Nicholas L Johnson. Instability of the present leo satellite populations. *Advances in Space Research*, 41(7):1046–1053, 2008.
- [2] Donald J. Kessler and Burton G. Cour-Palais. Collision frequency of artificial satellites: The creation of a debris belt. *Journal of Geophysical Research*, 83(A6):2637–2646, 1978.
- [3] J-C Liou, Nicholas L Johnson, and NM Hill. Controlling the growth of future leo debris populations with active debris removal. *Acta Astronautica*, 66(5-6):648–653, 2010.
- [4] TS Kelso. Analysis of the iridium 33-cosmos 2251 collision. *Advances in the Astronautical Sciences*, 135(2):1099–1112, 2009.
- [5] Rémi Soulard, Mark N. Quinn, Toshiki Tajima, and Gérard Mourou. Ican: A novel laser architecture for space debris removal. *Acta Astronautica*, 105(1):192–200, 2014.
- [6] Claudio Bombardelli and Jesus Pelaez. Ion beam shepherd for contactless space debris removal. *Journal of guidance, control, and dynamics*, 34(3):916–920, 2011.
- [7] Markus Wilde, Ian Walker, Stephen Kwok Choon, and James Near. Using tentacle robots for capturing non-cooperative space debris-a proof of concept. In *AIAA SPACE and Astronautics Forum and Exposition*, page 5246, 2017.
- [8] Kenji Nagaoka, Ryota Kameoka, and Kazuya Yoshida. Repeated impact-based capture of a spinning object by a dual-arm space robot. *Frontiers in Robotics and AI*, 5:115, 2018.
- [9] Vladimir S. Aslanov and Vadim V. Yudintsev. Behavior of tethered debris with flexible appendages. *Acta Astronautica*, 104(1):91–98, 2014.

- [10] Roger Dudziak, Sean Tuttle, and Simon Barracough. Harpoon technology development for the active removal of space debris. *Advances in Space Research*, 56(3):509–527, 2015.
- [11] Inna Sharf, Benjamin Thomsen, Eleonora M. Botta, and Arun K. Misra. Experiments and simulation of a net closing mechanism for tether-net capture of space debris. *Acta Astronautica*, 139:332–343, 2017.
- [12] G. S. Aglietti, B. Taylor, S. Fellowes, S. Ainley, D. Tye, C. Cox, A. Zarkesh, A. Mafficini, N. Vinkoff, K. Bashford, T. Salmon, I. Retat, C. Burgess, A. Hall, T. Chabot, K. Kanani, A. Pisseloup, C. Bernal, F. Chaumette, A. Pollini, and W. H. Steyn. Removedebris: An in-orbit demonstration of technologies for the removal of space debris. *The Aeronautical Journal*, 124(1271):1–23, 2019.
- [13] Eleonora M. Botta, Corey Miles, and Inna Sharf. Simulation and tension control of a tether-actuated closing mechanism for net-based capture of space debris. *Acta Astronautica*, 174:347–358, 2020.
- [14] Minghe Shan, Jian Guo, and Eberhard Gill. Review and comparison of active space debris capturing and removal methods. *Progress in Aerospace Sciences*, 80:18–32, 2016.
- [15] PengYuan Zhao, JinGuo Liu, and ChenChen Wu. Survey on research and development of on-orbit active debris removal methods. *Science China Technological Sciences*, 63(11):2188–2210, 2020.
- [16] Eleonora M. Botta. *Deployment and Capture Dynamics of Tether-Nets for Active Space Debris Removal*. Thesis, McGill University, 2017.
- [17] Man Ru, Ying Zhan, Bin Cheng, and Yu Zhang. Capture dynamics and control of a flexible net for space debris removal. *Aerospace*, 9(6):299, 2022.
- [18] Dmitry A Sizov and Vladimir S Aslanov. Space debris removal with harpoon assistance: Choice of parameters and optimization. *Journal of Guidance, Control, and Dynamics*, 44(4):767–778, 2020.
- [19] Wei Zhao, Zhaojun Pang, Zhen Zhao, Zhonghua Du, and Weiliang Zhu. A simulation and an experimental study of space harpoon low-velocity impact, anchored debris. *Materials*, 15(14):5041, 2022.
- [20] Yuto Tamaki and Hiroaki Tanaka. Experimental study on penetration characteristics of metal harpoons with various tip shapes for capturing space debris. *Advances in Space Research*, 2022.

- [21] Panfeng Huang, Dongke Wang, Zhongjie Meng, Fan Zhang, and Zhengxiang Liu. Impact dynamic modeling and adaptive target capturing control for tethered space robots with uncertainties. *IEEE/ASME Transactions on Mechatronics*, 21(5):2260–2271, 2016.
- [22] Bingheng Wang, Zhongjie Meng, and Panfeng Huang. Attitude control of towed space debris using only tether. *Acta Astronautica*, 138:152–167, 2017.
- [23] William J. O'Connor and Deborah J. Hayden. Detumbling of space debris by a net and elastic tether. *Journal of Guidance, Control, and Dynamics*, 40(7):1832–1839, 2017.
- [24] Zhiping Zhang, Zhiwei Yu, Qianwen Zhang, Ming Zeng, and Shunli Li. Dynamics and control of a tethered space-tug system using takagi-sugeno fuzzy methods. *Aerospace Science and Technology*, 87:289–299, 2019.
- [25] Xin Sun and Rui Zhong. Nutation damping and spin orientation control of tethered space debris. *Acta Astronautica*, 160:683–693, 2019.
- [26] Minghe Shan, Jian Guo, and Eberhard Gill. Contact dynamics on net capturing of tumbling space debris. *Journal of Guidance, Control, and Dynamics*, 41(9):2063–2072, 2018.
- [27] Eleonora M Botta, Inna Sharf, and AK Misra. Evaluation of net capture of space debris in multiple mission scenarios. In *26th AAS/AIAA Space Flight Mechanics Meeting, Napa, CA*, pages 16–254. AAS, 2016.
- [28] Eleonora M. Botta, Inna Sharf, Arun K. Misra, and Marek Teichmann. On the simulation of tether-nets for space debris capture with vortex dynamics. *Acta Astronautica*, 123:91–102, 2016.
- [29] Guglielmo S Aglietti, Ben Taylor, Simon Fellowes, Thierry Salmon, Ingo Retat, Alexander Hall, Thomas Chabot, Aurélien Pisseloup, Christopher Cox, and A Mafficini. The active space debris removal mission removedebris. part 2: In orbit operations. *Acta Astronautica*, 168:310–322, 2020.
- [30] Vladimir S. Aslanov and Vadim V. Yudintsev. Dynamics of large debris connected to space tug by a tether. *Journal of Guidance, Control, and Dynamics*, 36(6):1654–1660, 2013.
- [31] Vladimir S. Aslanov and Vadim V. Yudintsev. Chaos in tethered tug–debris system induced by attitude oscillations of debris. *Journal of Guidance, Control, and Dynamics*, 42(7):1630–1637, 2019.
- [32] Riccardo Benvenuto, Samuele Salvi, and Michèle Lavagna. Dynamics analysis and gnc design of flexible systems for space debris active removal. *Acta Astronautica*, 110:247–265, 2015.

- [33] Kirk Hovell and Steve Ulrich. Attitude stabilization of an uncooperative spacecraft in an orbital environment using visco-elastic tethers. *AIAA Guidance, Navigation, and Control Conference*, 2016.
- [34] Sean Cleary and William J O'Connor. Control of space debris using an elastic tether and wave-based control. *Journal of Guidance, Control, and Dynamics*, 39(6):1392–1406, 2016.
- [35] T. V. Peters, José Francisco Briz Valero, Diego Escorial Olmos, V. Lappas, P. Jakowski, I. Gray, A. Tsourdos, H. Schaub, and R. Biesbroek. Attitude control analysis of tethered de-orbiting. *Acta Astronautica*, 146:316–331, 2018.
- [36] Minghe Shan and Lingling Shi. Velocity-based detumbling strategy for a post-capture tethered net system. *Advances in Space Research*, 70(5):1336–1350, 2022.
- [37] Minghe Shan and Lingling Shi. Comparison of tethered post-capture system models for space debris removal. *Aerospace*, 9(1), 2022.
- [38] H. T. K. Linskens and E. Mooij. Tether dynamics analysis and guidance and control design for active space-debris removal. *Journal of Guidance, Control, and Dynamics*, 39(6):1232–1243, 2016.
- [39] Marco Sabatini, Paolo Gasbarri, and Giovanni B Palmerini. Elastic issues and vibration reduction in a tethered deorbiting mission. *Advances in Space Research*, 57(9):1951–1964, 2016.
- [40] Zhongjie Meng, Bingheng Wang, and Panfeng Huang. Twist suppression method of tethered towing for spinning space debris. *Journal of Aerospace Engineering*, 30(4), 2017.
- [41] Riccardo Benvenuto, Michèle Lavagna, A Cingoli, C Yabar, and M Casasco. Must: Multi-body dynamics simulation tool to support the gnc design for active debris removal with flexible elements. In *Proc. 9th International ESA Conference on Guidance, Navigation & Control Systems, Porto, Portugal*, 2016.
- [42] Lee Jasper and Hanspeter Schaub. Tethered towing using open-loop input-shaping and discrete thrust levels. *Acta Astronautica*, 105(1):373–384, 2014.
- [43] Paweł Jaworski, Vaios Lappas, Antonios Tsourdos, Iain Gray, and Hanspeter Schaub. Debris rotation analysis during tethered towing for active debris removal. *Journal of Guidance, Control, and Dynamics*, 40(7):1769–1778, 2017.

- [44] John L. Crassidis, Srinivas R. Vadali, and F. Landis Markley. Optimal variable-structure control tracking of spacecraft maneuvers. *Journal of Guidance, Control, and Dynamics*, 23(3):564–566, 2000.
- [45] Jiyue Si, Zhaojun Pang, Zhonghua Du, and Chun Cheng. Dynamics modeling and simulation of self-collision of tether-net for space debris removal. *Advances in Space Research*, 64(9):1675–1687, 2019.

ProQuest Number: 29327231

INFORMATION TO ALL USERS

The quality and completeness of this reproduction is dependent on the quality
and completeness of the copy made available to ProQuest.



Distributed by ProQuest LLC (2022).

Copyright of the Dissertation is held by the Author unless otherwise noted.

This work may be used in accordance with the terms of the Creative Commons license
or other rights statement, as indicated in the copyright statement or in the metadata
associated with this work. Unless otherwise specified in the copyright statement
or the metadata, all rights are reserved by the copyright holder.

This work is protected against unauthorized copying under Title 17,
United States Code and other applicable copyright laws.

Microform Edition where available © ProQuest LLC. No reproduction or digitization
of the Microform Edition is authorized without permission of ProQuest LLC.

ProQuest LLC
789 East Eisenhower Parkway
P.O. Box 1346
Ann Arbor, MI 48106 - 1346 USA